J. Fluid Mech. (2019), *vol.* 875, *pp.* 657–698. © Cambridge University Press 2019
doi:10.1017/jfm.2019.488

Regime transitions and energetics of sustained stratified shear flows

Adrien Lefauve[1],†, **J. L. Partridge**[1] and **P. F. Linden**[1]

[1]Department of Applied Mathematics and Theoretical Physics, Centre for Mathematical Sciences, Wilberforce Road, Cambridge CB3 0WA, UK

(Received 11 January 2019; revised 7 June 2019; accepted 11 June 2019)

We describe the long-term dynamics of sustained stratified shear flows in the laboratory. The stratified inclined duct (SID) experiment sets up a two-layer exchange flow in an inclined duct connecting two reservoirs containing salt solutions of different densities. This flow is primarily characterised by two non-dimensional parameters: the tilt angle of the duct with respect to the horizontal, θ (a few degrees at most), and the Reynolds number Re, an input parameter based on the density difference driving the flow. The flow can be sustained with constant forcing over arbitrarily long times and exhibits a wealth of dynamical behaviours representative of geophysically relevant sustained stratified shear flows. Varying θ and Re leads to four qualitatively different regimes: laminar flow; mostly laminar flow with finite-amplitude, travelling Holmboe waves; spatio-temporally intermittent turbulence with substantial interfacial mixing; and sustained, vigorous interfacial turbulence (Meyer & Linden, *J. Fluid Mech.*, vol. 753, 2014, pp. 242–253). We seek to explain the scaling of the transitions between flow regimes in the two-dimensional plane of input parameters (θ, Re). We improve upon previous studies of this problem by providing a firm physical basis and non-dimensional scaling laws that are mutually consistent and in good agreement with the empirical transition curves we inferred from 360 experiments spanning $\theta \in [-1^\circ, 6^\circ]$ and $Re \in [300, 5000]$. To do so, we employ state-of-the-art simultaneous volumetric measurements of the density field and the three-component velocity field, and analyse these experimental data using time- and volume-averaged potential and kinetic energy budgets. We show that regime transitions are caused by an increase in the non-dimensional time- and volume-averaged kinetic energy dissipation within the duct, which scales with θRe at high enough angles. As the power input scaling with θRe is increased above zero, the two-dimensional, parallel-flow dissipation (power output) increases to close the budget through an increase in the magnitude of the exchange flow, incidentally triggering Holmboe waves above a certain threshold in interfacial shear. However, once the hydraulic limit of two-layer exchange flows is reached, two-dimensional dissipation plateaus and three-dimensional dissipation at small scales (turbulence) takes over, at first intermittently, and then steadily, in order to close the budget and follow the θRe scaling. This general understanding of regime transitions and energetics in the SID experiment may serve as a basis for the study of more complex sustained stratified shear flows found in the natural environment.

Key words: stratified flows, stratified turbulence, turbulent transition

---

† Email address for correspondence: lefauve@damtp.cam.ac.uk

1. Introduction

Turbulence is still an ‘unsolved problem’, and the stabilising buoyancy forces that characterise stratified turbulence add further complexity. The range of spatio-temporal scales involved in the physics of (stratified) turbulent flows make them difficult to simulate with our current computational capabilities. Stably stratified shear flows are a class of flows particularly relevant to the environment. Many of these flows are sustained over long periods of time through quasi-steady forcing: for example, exchange flows in straits (Armi & Farmer 1988), estuaries (Geyer *et al.* 2010), coastal inlets (Farmer & Armi 1999), deep ocean overflows (van Haren *et al.* 2014), the wind-driven equatorial undercurrent (Gregg *et al.* 1985) and the atmospheric boundary layer (Mahrt 2014). In this paper, we address these general and geophysically relevant sustained stratified shear flows using a simple laboratory experiment.

The stratified inclined duct experiment (hereafter abbreviated SID), sketched in figure 1, consists of two reservoirs initially filled with aqueous salt solutions of different densities $\rho_0 \pm \Delta\rho/2$, connected by a long rectangular duct that can be tilted at a small angle θ from the horizontal. At the start of the experiment, the duct is opened, initiating a brief transient gravity current followed by a two-layer exchange flow in the duct that is sustained for long periods of time. This sustained stratified shear flow is the focus of this paper.

Previous studies of this experiment highlighted the fact that the flow exhibits qualitatively different regimes depending on the input parameters θ and $\Delta\rho$. In this paper, we adopt the nomenclature of Meyer & Linden (2014) who described the four following regimes based on simple shadowgraph observations (see their figure 3):

L : laminar steady flow, with a thin, flat density interface between the two counter-flowing layers;

H : mostly laminar flow, with finite-amplitude Holmboe waves propagating on the interface;

I : spatio-temporally intermittent turbulence with small-scale structures and mixing;

T : steadily sustained turbulence with significant small-scale structures and a thick interfacial mixing layer.

Stratified turbulence research has traditionally focused on the modelling of the ‘small-scale’ (inaccessible) physics of mixing using the ‘large-scale’ (accessible) properties of the flows. A much-pursued goal is the ability to predict the regime of any given flow (e.g. laminar, intermittently turbulent, fully turbulent), its rate of energy dissipation and its mixing efficiency (so-called ‘output’ variables) using only a small number of ‘input’ non-dimensional parameters characterising the flow (for four decades of reviews on mixing efficiency, see e.g. Linden (1979), Fernando (1991), Ivey, Winters & Koseff (2008), Gregg *et al.* (2018)). To achieve this goal, scaling laws obtained from a physical model (based on the Navier–Stokes equations) are usually required to extrapolate empirical relationships obtained under controlled laboratory conditions to the geophysical scales of ultimate interest.

This paper follows this tradition of research and elaborates on ideas developed in previous studies – in particular Meyer & Linden (2014) – to tackle the non-dimensional scaling laws describing transitions between flow regimes. In this paper, we revisit these ideas in order to provide a more physical and quantitative explanation of regime transitions in the SID experiment. To achieve this aim, we use (i) newly available volumetric measurements of the three-dimensional density field and three-component velocity field, and (ii) a volume-averaged energetics model suited to the analysis of these measurements.

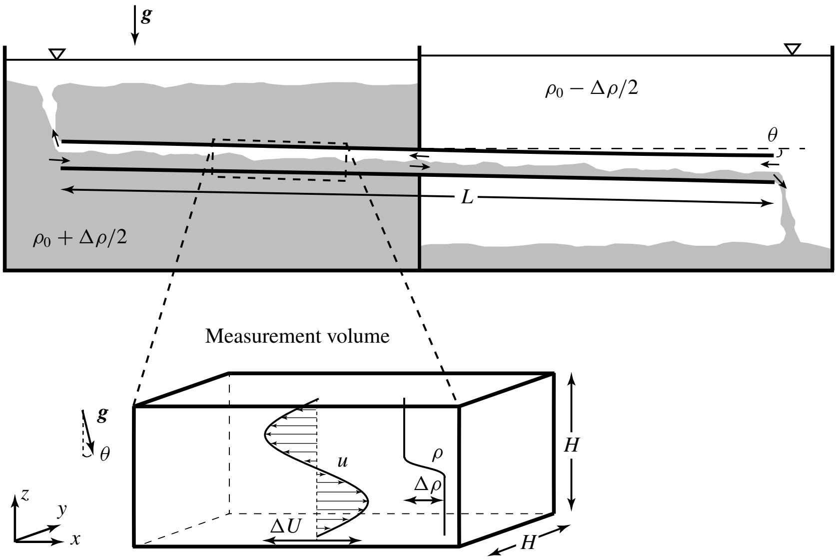

FIGURE 1. Schematics of the stratified inclined duct (SID) experiment. The measurement volume inset shows the coordinate system and the notation used in this paper (in dimensional units). Note that the x axis is aligned along the duct, resulting in gravity pointing at an angle θ from the $-z$ direction. Here, by definition, the duct is inclined at a positive angle $\theta > 0°$, resulting in a positive forcing of the flow by the streamwise projection of gravity $g \sin\theta > 0$.

The rest of the paper is organised as follows. In § 2 we provide the background for the non-dimensional study of the SID experiment and discuss previous studies together with new data on regime transitions in order to motivate the need to revisit this problem. In § 3 we introduce our new volumetric measurements and use them to visualise and further characterise all four flow regimes. In § 4 we derive from first principles a framework of energy budgets suited to our volumetric measurements. In § 5, we validate the framework and its predictions for regime transitions with experimental data. In § 6, we further develop this framework and the analysis of experimental data to study the relation between flow regimes and three-dimensionality. Finally, we summarise our findings and discuss open questions in § 7.

2. Background

In this section, we introduce our notation in § 2.1, and discuss in § 2.2 the scaling of streamwise velocities important for the non-dimensionalisation of the problem in § 2.3. We then discuss the scaling laws for the regime transitions proposed by previous studies in § 2.4, before presenting new data to motivate the paper in § 2.5.

2.1. *Notation*

Our notation is shown in the measurement volume inset in figure 1 and largely follows that of Lefauve *et al.* (2018) (hereafter LPZCDL18). The duct considered in this paper has length $L = 1350$ mm and a square cross-section of height and width $H = 45$ mm (the same dimensions as LPZCDL18 but smaller than ML14). The streamwise x axis is aligned along the duct and the spanwise y axis across the duct, making the z axis tilted at an angle θ from the vertical (resulting in a non-zero streamwise projection of gravity $g\sin\theta$). All coordinates are centred in the middle of the duct, such that $-L/2 \leqslant x \leqslant L/2$ and $-H/2 \leqslant y, z \leqslant H/2$. The velocity vector field has components $\boldsymbol{u}(x, y, z, t) = (u, v, w)$ along x, y, z, and we denote the density field by $\rho(x, y, z, t)$.

The parameters believed to play important roles are the geometrical parameters: L, H, θ and the dynamical parameters: the reduced gravity $g' \equiv g\Delta\rho/\rho_0$ (under the Boussinesq approximation of small density differences $0 < \Delta\rho/\rho_0 \ll 1$), the kinematic viscosity of water $\nu = 1.05 \times 10^{-6}\ \mathrm{m^2\ s^{-1}}$ and the molecular diffusivity of salt $\kappa_s = 1.50 \times 10^{-9}\ \mathrm{m^2\ s^{-1}}$. The last important parameter is the scale of the streamwise velocity ΔU, but it is not independent from the previous six parameters as we discuss in § 2.2. From these seven parameters having two dimensions (of length and time), we construct five independent non-dimensional parameters in § 2.3.

2.2. *Scaling of the velocity*

Meyer & Linden (2014) recognised that the two-layer exchange flow in the SID is maximal because it is hydraulically controlled at both ends of the duct where it meets the reservoirs through a sharp change in geometry (an idea already present in Wilkinson (1986)). In other words, the flow is subcritical with respect to long interfacial waves inside the duct (information propagates in both directions), and critical at either end, preventing the propagation of information (in particular of the exchange flow rate) from the exterior into the interior of the duct. The resulting flow is therefore said to be controlled by the interior and maximal in the sense that it has the largest exchange flow rate of any realisable flow (for more details, see ML14, Lefauve *et al.* 2018, § 3, and Lefauve 2018, § 1.3.2). This maximal exchange flow is sustained in a quasi-steady state until the controls are 'flooded' by the accumulation of fluid of a different density coming from the other reservoir. With each reservoir holding approximately 100 litres of fluid in our current set-up, a typical experiment can last several minutes, which represents many duct transit times (streamwise advection time along the length of the duct).

As a consequence, the velocity scale ΔU is not an independent parameter; it is set by the phase speed of long interfacial gravity waves. To understand this, we follow the literature (see e.g. Armi (1986), Lawrence (1990)) and consider the composite Froude number of this two-layer flow as

$$G^2(x) \equiv F_1^2(x) + F_2^2(x), \quad \text{where } F_i^2(x) \equiv \frac{\langle u_i^2(x)\rangle_{y,z_i}}{g' h_i(x)} \tag{2.1}$$

is the Froude number of layer i, $\langle\cdot\rangle_{y,z_i}$ denotes spanwise and vertical averaging over the depth h_i of each layer and the symbol $\equiv$ denotes a definition. In the idealised case of frictionless, horizontal ducts ($\theta = 0°$), the flow is streamwise invariant and G takes everywhere the value at the centre of the duct

$$G(x) = G(0) = 2\frac{\langle |u|\rangle_{y,z}}{\sqrt{g'H}}, \tag{2.2}$$

where $\langle\cdot\rangle_{y,z}$ denotes averaging over the whole duct cross-section. The second equality results from (2.1) and the symmetry of the flow at $x = 0$ guaranteed by the Boussinesq approximation ($\langle |u_1|\rangle_{y,z} = \langle |u_2|\rangle_{y,z}$ and $h_1 = h_2 = H/2$). Note that here and in the remainder of the paper, we assume that the exchange flow has zero net (or 'barotropic') flow rate $\langle u\rangle_{y,z} = 0$, which is a good approximation in the present set-up. Hydraulic control requires that $G^2 = 1$ (Armi 1986), which gives the following layer-averaged velocity

$$\langle |u| \rangle_{y,z} = \frac{\sqrt{g'H}}{2}, \tag{2.3}$$

as previously recognised by ML14. With the addition of viscous friction and/or of a non-zero tilt angle, the flow is no longer streamwise invariant: $G(x)$ is maximal at the ends ($x = \pm L/2$) and minimal in the centre ($x = 0$). Since the criticality condition $G^2 = 1$ is imposed at the ends where the controls occur $G(\pm L/2) = 1 > G(0)$, the velocity scale $\langle |u| \rangle_{y,z} = (\sqrt{g'H}/2)G(0)$ is lower than the inviscid upper bound (2.3) that we call the 'hydraulic limit' (see Gu & Lawrence (2005) for more details). As first observed in ML14 (see their figure 7) and as we shall substantiate in § 4.3.1, this hydraulic limit is however generally achieved when a positive tilt angle $\theta > 0^\circ$ is added to counterbalance the dissipative effects of viscosity.

Due to the moderate Reynolds numbers and the long duct investigated in the present set-up, the velocity profiles are usually significantly affected by viscosity in the sense that viscous boundary layers at the walls and interface are partially or fully developed. Generally, we find that the peak velocities in each layer are at most around twice the layer-averaged values corresponding to the hydraulic limit (2.3), i.e. $\max_{y,z} |u| \approx 2\langle |u| \rangle_{y,z} \approx \sqrt{g'H}$. We therefore choose to non-dimensionalise velocities by this characteristic 'peak' value, i.e. half the total (peak-to-peak) velocity jump (shown in the inset in figure 1):

$$\frac{\Delta U}{2} \equiv \sqrt{g'H}. \tag{2.4}$$

2.3. *Non-dimensionalisation*

Based on the above, we define the non-dimensional velocity vector as $\tilde{\boldsymbol{u}} \equiv \boldsymbol{u}/(\Delta U/2)$ such that in general $-1 \lesssim \tilde{u} \lesssim 1$ (noting that the streamwise velocity is dominant in this flow, i.e. $|\tilde{u}| \gg |\tilde{v}|, |\tilde{w}|$). For consistency, we choose $H/2$ as the length scale, defining the non-dimensional position vector as $\tilde{\boldsymbol{x}} \equiv \boldsymbol{x}/(H/2)$ such that $-1 \leqslant \tilde{y}, \tilde{z} \leqslant 1$, and $-A \leqslant \tilde{x} \leqslant A$, where the aspect ratio of the duct is

$$A \equiv \frac{L}{H}. \tag{2.5}$$

Consequently, we non-dimensionalise time by the advective time unit $H/\Delta U = 1/(2\sqrt{g'/H})$: $\tilde{t} \equiv 2\sqrt{g'/H}t$ (hereafter abbreviated ATU). The dimensionless density field is defined as $\tilde{\rho} \equiv (\rho - \rho_0)/(\Delta\rho/2)$, such that $-1 \leqslant \tilde{\rho} \leqslant 1$.

Using the previously defined velocity and length scales, we construct the Reynolds number

$$Re \equiv \frac{\dfrac{\Delta U}{2}\dfrac{H}{2}}{\nu} = \frac{\sqrt{g'H}H}{2\nu} = 1.42 \times 10^4 \sqrt{\frac{\Delta\rho}{\rho_0}}, \tag{2.6}$$

where the last equality shows that Re is a function of the driving density difference $\Delta\rho/\rho_0$ alone (the prefactor only holds for aqueous salt solutions in the geometry investigated here). In this paper, we present experiments in the range $\Delta\rho/\rho_0 \in [5 \times 10^{-4}, 1.3 \times 10^{-1}]$, i.e. $Re \in [300, 5000]$.

The velocity scale ΔU leads to the definition of an overall bulk Richardson number Ri_B, expressed as the non-dimensional product of the density, length and inverse square velocity scales, and which here takes a constant value

$$Ri_B \equiv \frac{\dfrac{g}{\rho_0}\dfrac{\Delta\rho}{2}\dfrac{H}{2}}{\left(\dfrac{\Delta U}{2}\right)^2} = \frac{1}{4}, \tag{2.7}$$

by criticality of the exchange flow and our definition of ΔU in (2.4).

Our last non-dimensional parameter is the Schmidt number, the ratio of the momentum to salt diffusivity

$$Sc \equiv \frac{\nu}{\kappa_s}. \tag{2.8}$$

In summary, we have a total of four free independent non-dimensional input parameters: θ, A, Re, Sc, and one imposed parameter Ri_B. For the apparatus considered, we have $A = 30$, $Sc = 700$, $Ri_B = 1/4$, and we have the freedom to vary θ and Re (by varying $\Delta\rho/\rho_0$), allowing us to access all flow regimes.

Henceforth, we drop the tildes and, unless explicitly stated otherwise, use non-dimensional variables throughout.

2.4. *Previous studies*

Meyer & Linden (2014) (ML14) mapped the distribution of the four regimes described in § 1 in the $\theta - \Delta\rho/(2\rho_0)$ plane for 93 experiments (see their figure 5). They sought an equation for the transition curves by arguing that, because of the presence of hydraulic controls (§ 2.2), the kinetic energy in the flow was bounded by the scaling $(\Delta U)^2 \sim g'H$ (see (2.3) and (2.4)) and thus it could not increase even in the presence of gravitational forcing when $\theta > 0°$. The dimensional 'excess kinetic energy' $g'L\sin\theta$, gained by conversion from potential energy by the fluid travelling a distance L along the duct in the streamwise field of gravity $g'\sin\theta > 0$, thus has to be dissipated by increased wave activity or turbulence. They non-dimensionalised this excess kinetic energy by $(\nu/H)^2$, thus forming the following Grashof number

$$Gr \equiv \frac{g'L\sin\theta}{(\nu/H)^2} = 4A\sin\theta Re^2, \tag{2.9}$$

where the first equality is their definition and the second equality uses our notation. They found reasonable agreement between this scaling in $\sin\theta Re^2$ (using two different aspect ratios $A = 15$, 30) and suggested the empirical equation $Gr = 4\times10^7$ for the $\mathsf{I}\rightarrow\mathsf{T}$ transition curve (see their figure 8). The limitations of this proposed Gr scaling will be discussed in § 2.5.

Macagno & Rouse (1961) (MR61) is the first study of the SID we are aware of. They mapped the same four regimes independently rediscovered by ML14 in a two-dimensional space (see their figure 8), but instead of using the two natural input parameters θ and Re emerging from the above dimensional analysis, they used a Froude number and a Reynolds number based on measured values of the actual (output) ΔU and of the vertical distance between the two maxima of $|u|$ (depth of the shear layer). They varied θ in non-trivial ways, sometimes during an experiment, in order to obtain target values of ΔU and therefore better control their Reynolds number, and did not appear to realise the presence and importance of hydraulic controls (in fact, they may have disturbed them by their use of splitter plates at the ends of the duct). The main limitation of MR61 is that they did not recognise the importance of θ in the regime transitions, and were thus unable to propose a convincing physical model to substantiate them.

Kiel (1991) (K91) proposed a heuristic scaling based on a 'geometric Richardson number' Ri_G, whose inverse (using our notation)

$$Ri_G^{-1} \equiv 4A \tan\theta + \tfrac{16}{9} \tag{2.10}$$

can be interpreted as the non-dimensionalisation of the 'excess kinetic energy' $g'L \sin\theta$ of ML14 by the actual kinetic energy of the hydraulically controlled flow $(\Delta U)^2 = g'H$, i.e. $Ri_G^{-1} \sim g'L\sin\theta/(g'H) = A\sin\theta$ (disregarding constants). He argued that transition to turbulence occurs when the excess energy to be dissipated becomes large compared to the maximum kinetic energy of the flow (high Ri_G^{-1}). The main limitation of K91 in the context of the present study is that he intentionally focused on large Re and assumed that viscous effects could be ignored. Although K91 did use large Re (of order 10^4) using ducts of dimensions similar to that of ML14, the observations of ML14 at similar Re highlight the importance of Re in the scaling, which we substantiate in this paper. Consequently, this Ri_G criterion is not sufficient to explain regime transitions.

2.5. *Observed regime transitions and motivation*

To further motivate the need to revisit the problem of regime transitions, we reproduced the regime diagram of ML14 in a slightly different duct geometry in figure 2. The duct used in this paper had a smaller cross-section than that used by ML14 ($H = 45$ mm versus 100 mm), but had the same aspect ratio $A = 30$ as that used by ML14 to obtain most of their data. We visually identified the four regimes L, H, I, T for a total of 360 experiments corresponding to different (θ, Re) couples. Out of these, 312 data points come from shadowgraph observations (as in ML14), 35 come from the volumetric measurements of density and velocity described in § 3 and 13 come from simpler planar measurements that were carried out before the volumetric system was operational (these measurements are not discussed in this paper).

We observe that the regimes largely occupy distinct regions of the $\theta - Re$ plane with clear boundaries that are simple open curves, which we refer to as the $\mathsf{L} \rightarrow \mathsf{H}$, $\mathsf{H} \rightarrow \mathsf{I}$, and $\mathsf{I} \rightarrow \mathsf{T}$ transitions. To fix ideas, we may formally define a 'regime function' reg taking arbitrary but increasing values such as

$$\mathrm{reg} \equiv 1 \text{ for } \mathsf{L}, \quad 2 \text{ for } \mathsf{H}, \quad 3 \text{ for } \mathsf{I}, \quad 4 \text{ for } \mathsf{T}. \tag{2.11a–d}$$

Finding the scaling of regime transitions is equivalent to finding the functional dependence of $\mathrm{reg}(\theta, Re)$, with 'transition curves' being described, for example, by the equations $\mathrm{reg} = 1.5, 2.5, 3.5$. Although sufficiently far from the transition curves, the flow regime is repeatable for a given (θ, Re), we observe a slight overlap between regimes near the transitions which could be explained by two potential reasons:

(i) the flow regime may not be a reproducible characteristic of the experiment (and of the underlying dynamical system) near the transitions due to its sensitivity to flow parameters, and/or to initial conditions (the initial transients resulting from the way the experiment is started, which cannot be controlled accurately);

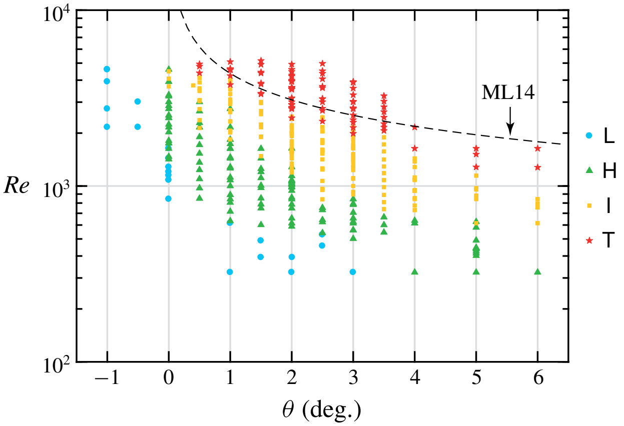

FIGURE 2. (Colour online) Regime diagram in the (θ, Re) plane of non-dimensional input parameters totalling 360 data points (most were determined from shadowgraph observations). In dashed, the I → T transition curve inferred by ML14 from their experiments in a larger duct.

(ii) the qualitative (visual) identification of flow regimes, i.e. the very definition of 'flow regime', is not appropriate near the transitions (i.e. not fine or consistent enough) to classify the flow into the four discrete categories of ML14.

Note that throughout this paper, we use the term transition to refer to the change in the qualitative long-term (asymptotic) dynamics of the flow caused by changes in the input parameters. Although mathematically such behaviour is typically referred to as a bifurcation, we chose to avoid this term in this paper since we do not prove nor imply that the underlying dynamical system indeed exhibits strict bifurcations. This question is interesting but outside the scope of this paper.

The I → T transition curve proposed by ML14 (see § 2.4) is reproduced in dashed black in figure 2 to highlight the fact that the agreement in our geometry (smaller duct) is less convincing. The ML14 curve lies entirely in the T region (i.e. it is 'too high') and the discrepancy is particularly apparent at higher angles $\theta \gtrsim 4^\circ$ (which were not considered by ML14), suggesting that their proposed $Gr \sim \sin\theta Re^2$ scaling may not be universal.

To summarise, we have seen that regime transitions in the SID depend on at least two input parameters: θ and Re. The first two attempts to understand the transitions (MR61 and K91) each ignored one of them, proposing heuristic scalings based on (respectively) either Re or θ. More recently, ML14 correctly identified the $\theta - Re$ dependence, understood the role of hydraulic controls and proposed a transition scaling following $Gr \sim \sin\,\theta Re^2 = \text{const.}$ (see (2.9)). This scaling was based on physical arguments of excess kinetic energy, which, as we will show in this paper, are essentially correct but will be made more specific. However, the first limitation of this Gr criterion is that the non-dimensionalisation of the excess kinetic energy by the square velocity scale $(\nu/H)^2$ leading to the Grashof number Gr is not justifiable by physical principles, and subsequently nor is the value $Gr = 4 \times 10^7$ for the I → T transition. The second limitation of the Gr criterion is that it does not appear to agree with our more recent and comprehensive data obtained in a smaller duct (figure 2).

We believe that these limitations motivate the need for a revised scaling of regime transitions of the form $\text{reg}(\theta, Re) = \text{const.}$ verified by quantitative experimental data and based on sound physical principles.

In the next two sections we introduce the experimental measurements (§ 3) and physical model (§ 4) employed to achieve this aim.

3. Measurements and visualisations

In this section, we describe our volumetric measurements of the three-dimensional density field and three-component velocity field in § 3.1. We then use these measurements for quantitative flow visualisations in each of the four regimes in § 3.2 to highlight their key features and build intuition.

3.1. *Three-dimensional, three-component (3D-3C) measurements*

To provide a quantitative basis to the qualitative shadowgraph observations and subsequent categorisation into flow regimes, we investigate in this paper the detailed energetics underpinning each regime. To do so, we employed simultaneous measurements of the density field and three-dimensional, three-component (3D-3C) velocity field in a volume, as sketched in the inset of figure 1.

These measurements relied on a novel technique introduced by Partridge, Lefauve & Dalziel (2019) in which a thin, pulsed vertical laser sheet (in the x–z plane) is scanned rapidly back and forth in the spanwise direction (along y) to span a duct sub-volume of non-dimensional cross-section 2×2 and non-dimensional length ℓ (typically a small fraction of full duct length $\ell \ll 2A$). Simultaneous stereo particle image velocimetry (sPIV) and planar laser induced fluorescence (PLIF) are employed to obtain the three-dimensional, three-component velocity and density fields $(u, v, w, \rho)(x, y_i, z, t_i)$ in successive x–z planes at spanwise locations $y = y_i$ and respective times $t = t_i$. Three-dimensional volumes containing n_y planes (i.e. $i = 1, 2, \ldots, n_y$) are then reconstructed from these plane measurements. These volumetric 3D-3C measurements are only near instantaneous in the sense that each plane (x, y_i, z, t_i) is separated from the previous one by a small time increment $\delta t \equiv t_i - t_{i-1}$, resulting in each volume being constructed over a non-dimensional time $\Delta t \equiv n_y \delta t$. The experimental protocol and details to obtain the measurements used in this paper are identical to those discussed in LPZCDL18 §§ 3.3–3.4, who first used this novel technique to investigate the structure of Holmboe waves found in the H regime.

This technique provides high-resolution measurements of $(u, v, w, \rho)(x, y, z, t)$ with a typical number of data points in each coordinate $(n_x, n_y, n_z, n_t) \approx (500, 30, 100, 300)$ per experiment (after processing 150 GB of raw data). The details of the volume location $\bar{x}$, length ℓ, duration of an experiment τ, and resolution $(\Delta x, \Delta y, \Delta z, \Delta t) \equiv (\ell/n_x, 2/n_y, 2/n_z, \tau/n_t)$ for all 3D-3C experiments discussed in this paper will be given in § 5 (table 2). We discuss the physical constraints setting bounds on all of the above resolutions in appendix A.

Finally, we enforced incompressibility in all 3D-3C velocity fields by imposing $\boldsymbol{\nabla}\boldsymbol{\cdot}\boldsymbol{u} = 0$ for each of the n_t volumes. We employed the recent weighted divergence correction scheme of Wang *et al.* (2017), which constitutes an improved and much faster variant of the general algorithm of de Silva, Philip & Marusic (2013). Encouragingly, we found that the level of correction needed (the volume-averaged relative L^2 distance between the original and corrected fields) was typically small (at most a few per cent).

3.2. *Visualisations*

Using the measurements described above, we show visualisations of a flow representative of each of the four regimes in figure 3 (L and H regimes) and figure 4 (I and T regimes). We compare side-by-side the same three types of data:

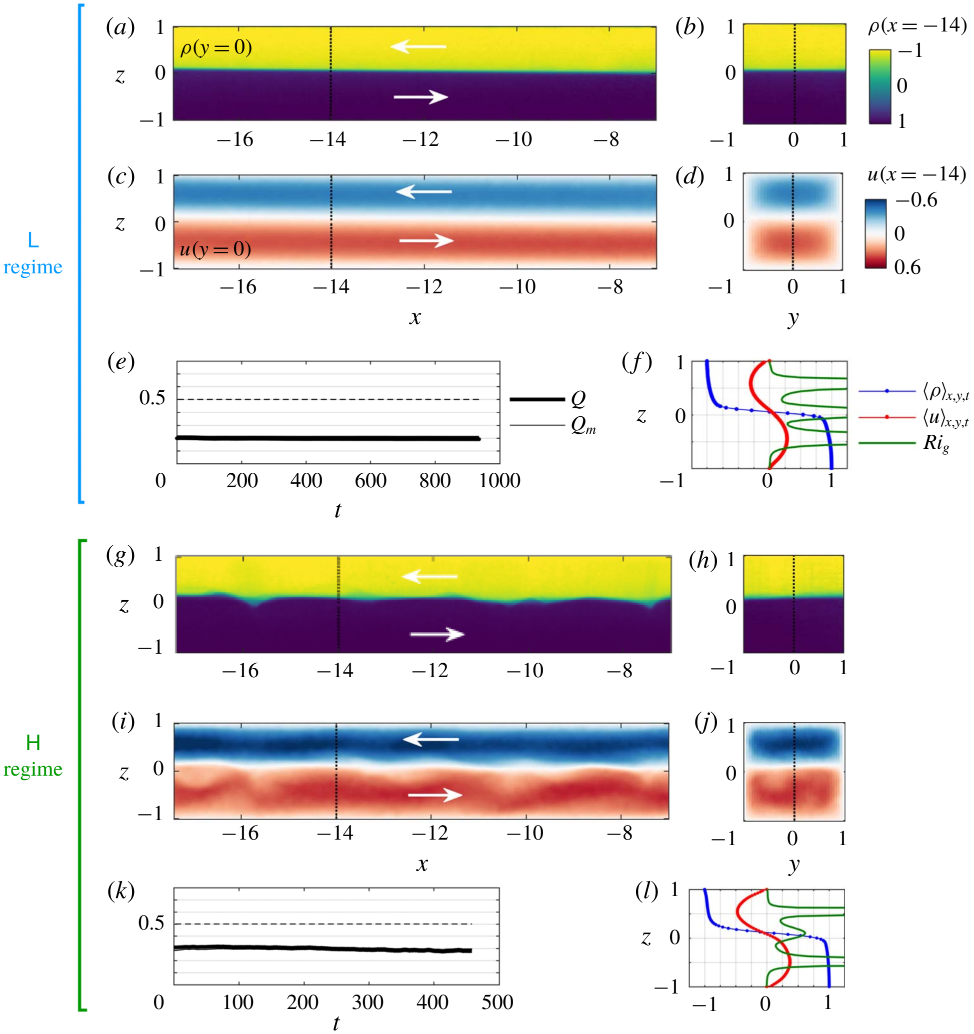

FIGURE 3. (Colour online) Comparative visualisations of a typical (*a–f*) L flow ($\theta = 2°$, $Re = 398$) and (*g–l*) H flow ($\theta = 1°$, $Re = 1455$). The I and T regimes are shown in figure 4. The L and H data correspond respectively to experiments L1 and H1 listed in table 2 (discussed later). For each experiment, we plot the density field ρ and streamwise velocity field u in (*a*,*c*,*g*,*i*) the vertical mid-plane of the volume $y=0$, and in (*b*,*d*,*h*,*j*) the arbitrary cross-sectional plane $x=-14$, all for a single arbitrary temporal snapshot: $t=150$ in (*a–d*), and $t=261$ in (*g–j*). Colour bars are identical for all plots showing density or velocity and are thus not repeated. Dotted vertical lines in the $y=0$ plane (*a*,*c*,*g*,*i*) indicate the location of the $x=-14$ plane in (*b*,*d*,*h*,*j*) and conversely. White arrows indicate the direction of the flow in each layer (in agreement with the notation of § 2.1 and figure 1). In addition, we plot for each experiment: (*e*,*k*) the temporal evolution of the volume flux $Q(t)$ and mass flux $Q_m(t)$ (the dashed line is the hydraulic limit $Q=0.5$); and (*f*,*l*) the mean vertical density, streamwise velocity and gradient Richardson number profiles (the dot symbols indicate the vertical resolution of the data).

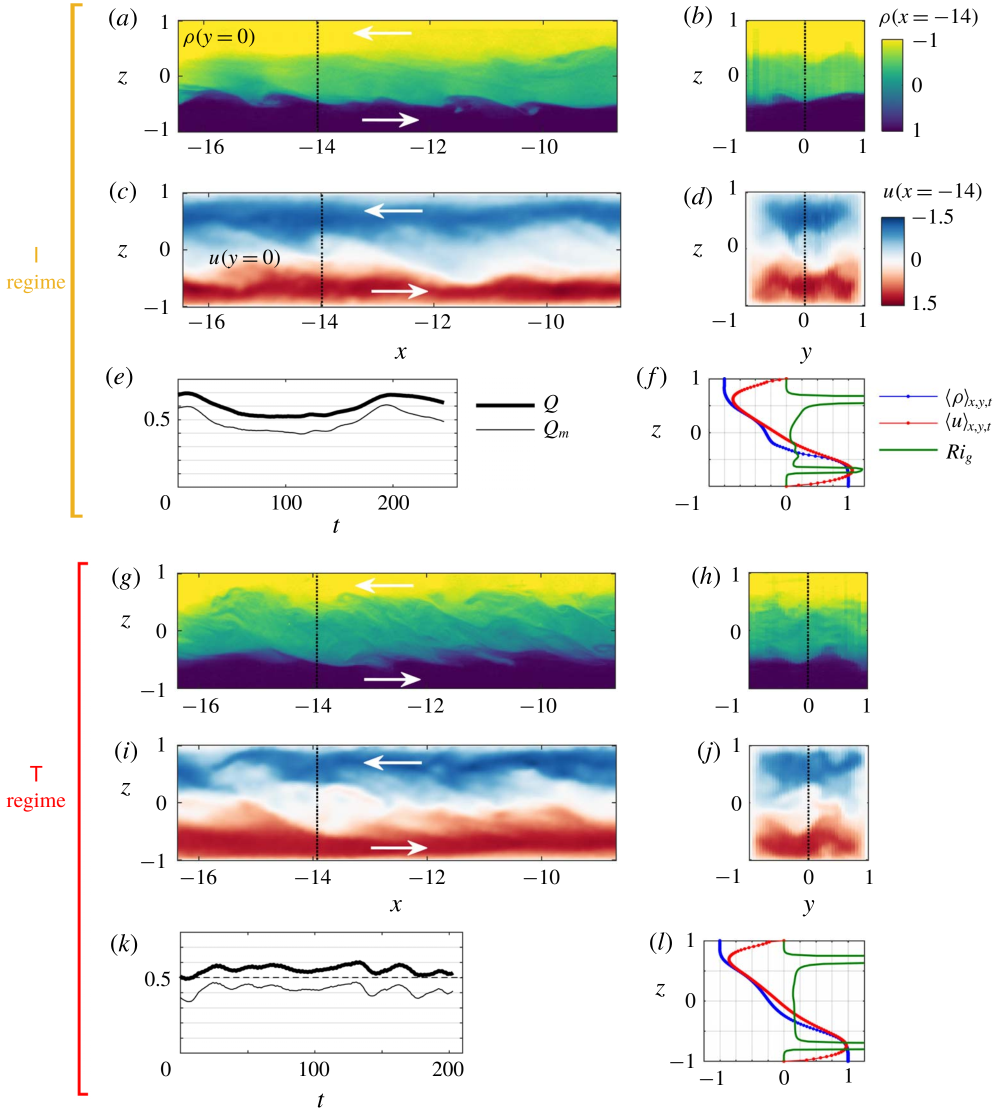

FIGURE 4. (Colour online) Comparative visualisations of a typical (*a*–*f*) I flow ($\theta = 6^\circ$, $Re = 777$) and (*g*–*l*) T flow ($\theta = 6^\circ$, $Re = 1256$), corresponding respectively to experiments I4 and T2 of table 2 (discussed later). The legend is identical to that of figure 3, except for the temporal snapshots used here: $t = 55$ in (*a*–*d*) and $t = 168$ in (*g*–*j*).

(i) an instantaneous snapshot of the density field ρ and streamwise velocity field u in the vertical mid-plane $y = 0$ of the measurement volume (panels *a*,*c*,*g*,*i*), and in the arbitrary cross-sectional plane $x = -14$ (panels *b*,*d*,*h*,*j*);

(ii) the averaged vertical density profile $\langle\rho\rangle_{x,y,t}(z)$, velocity profile $\langle u\rangle_{x,y,t}(z)$, and corresponding gradient Richardson number (panels *f*,*l*) defined as

$$Ri_g(z) \equiv -Ri_B \frac{\partial_z\langle\rho\rangle_{x,y,t}}{(\partial_z\langle u\rangle_{x,y,t})^2}; \tag{3.1}$$

(iii) the time series of the volume flux $Q(t)$ and mass flux $Q_m(t)$ (panels *e*,*k*) defined respectively as the exchange volume flow rate

$$Q(t) \equiv \langle |u| \rangle_{x,y,z}, \tag{3.2}$$

and the exchange mass flow rate

$$Q_m(t) \equiv \langle \rho u \rangle_{x,y,z}. \tag{3.3}$$

Note that $Q_m = Q$ in the absence of mixing (since in this case $\rho = \mathrm{sgn}(u)$), but in general $0 < Q_m < Q$ in the presence of mixing. The non-dimensional hydraulic limit for the volume flux set by the maximal exchange flow condition is $Q = 0.5$, such that in general $0 < Q_m \leqslant Q \leqslant 0.5$ (the first two inequalities always hold by definition whereas the last inequality is the hydraulic limit that does not precisely hold in the experiments).

We observe that the L and H flows have a sharp density interface with a tanh-like vertical profile (figure 3*a*,*b*,*f*,*g*,*h*,*l*), while the I and T flows have a mixing layer (figure 4*a*,*b*,*f*,*g*,*h*,*l*), i.e. a central layer in which the vertical density gradient is smaller than the values immediately above and below it as a result of turbulent mixing across the interface. As a result, in L and H flows, the gradient Richardson number (figure 3*l*) exhibits a local maximum at the density interface and two minima on either side of order $Ri_g \approx 0.25$ (L flow) and $Ri_g \approx 0.15 - 0.20$ (H flow). In the I flow, the local maximum at the interface largely disappears (figure 4*l*), where Ri_g is relatively constant across the shear layer and $Ri_g \approx 0.05 - 0.30$. In the T flow, Ri_g is very nearly constant throughout the shear layer at $Ri_g \approx 0.15$, in good agreement with the self-adjusting arguments of an ‘equilibrium Richardson number’ (Turner 1973, § 10.2) and of ‘marginal instability’ (Thorpe & Liu 2009; Smyth & Moum 2013).

In the L and H regimes, the streamwise velocity profile has a sine-like vertical structure (figure 3*f*,*l*) indicative of fully developed velocity boundary layers (expected when $Re \lesssim 50A = 1500$, the criterion for overlapping of the interfacial, top and bottom wall 99 % boundary layers at $x = 0$). By contrast, in the I and T regimes, interfacial turbulence creates a region of approximately constant velocity gradient across the mixing layer and ‘pointier’ velocity maxima that are pushed closer to the top and bottom walls (figure 4*f*,*l*) especially when turbulence is more intense and sustained in the T flow. In all regimes, these velocity maxima $\partial_z \langle u \rangle_{x,y,t} = 0$ at $|z| \approx 0.5 - 0.7$ caused by the no-slip condition at $z = \pm 1$ and the influence of viscosity account for the two symmetric peaks of Ri_g.

We also note that the L flow is largely (i) parallel, i.e. independent of the streamwise direction x, except for a very slight downward slope of the interface typical of such flows (discussed later in § 4.3.1); (ii) steady in time; (iii) symmetric about the $y = 0$ and $z = 0$ planes. By contrast, the H flow breaks the x- and t-invariance with a set of travelling, symmetric Holmboe waves distorting the density and velocity interfaces in a characteristic ‘cusp’-like pattern and in a quasi-periodic fashion (these ‘confined Holmboe waves’ were the focus of LPZCDL18). In addition, complex three-dimensional wave motions in the velocity field start breaking the $y = 0$ and $z = 0$ symmetries (figure 3*i*,*j*).

In the I and T flows, the departure from both the x, t invariances and the $y, z = 0$ symmetries at any instant in time is even greater, owing to large, three-dimensional turbulent fluctuations (figure 4). Based on the amplitude and spatial scales of the fluctuations in the position of the density and velocity interfaces, and the amplitude of the temporal fluctuations in the $Q(t)$ and $Q_m(t)$ time series, it is tempting to classify

	L	H	I	T
Invariance in x, t	✓	$\sim$	×	×
Symmetry about $y, z = 0$	✓	$\sim$	×	×
Large Q, $Q_m \approx 0.5$	×	×	✓	✓
Interfacial mixing	×	×	✓	✓
Small spatial scales	×	$\sim$	✓	✓
Constant interfacial Ri_g	×	×	$\sim$	✓
Laminar-turbulent periodicity	×	×	✓	×

TABLE 1. Basic characteristics of flow regimes inferred from figures 3–4. Symbol $\sim$ indicates a relatively small effect.

the L and H flows in one group based on their similarity, and the I and T regimes in a different group. The L – H flows have lower volume and mass flux, which are equal in the absence of mixing ($Q_m \approx Q \approx 0.2 - 0.3$), while the I – T flows have higher fluxes and significant mixing ($Q_m \approx 0.4 - 0.5 < Q \approx 0.5 - 0.6$, close to the hydraulic limit).

Large temporal fluctuations in both Q and Q_m are observed in the I and T regimes, but I flows tend to exhibit a component with longer pseudo-period associated with oscillations between laminar and turbulent events (sometimes in a quasi-periodic fashion with period $O(100$ ATU$)$). This is visible in the I flow here (figure 4*e*): the start of a turbulent event (shown here in the snapshots figure 4*a–d* at $t = 55$) follows the instability of an accelerating, largely laminar, three-layer flow. A peak in the volume flux at $t \approx 10$ triggered large-amplitude waves at both density interfaces which started overturning at $t \approx 40$ and initiated a turbulent event slowing down the flow (decreasing Q and Q_m). Relaminarisation followed at $t \approx 130$ (increasing Q and Q_m), and another cycle started (note that only one cycle was recorded here).

The basic characteristics of flow regimes described above are summarised in table 1. In the next section, we introduce the mathematical framework suited to analyse the above 3D-3C measurements and understand the energetics of SID flows.

4. Energetics model

In this section, we start by deriving the time evolution equations for the kinetic energy and potential energy, first as local quantities in § 4.1, and then averaged in a control volume in § 4.2. To jump to the result of this section, see (4.10) and (4.13) and figure 5. We then estimate the transfer terms between kinetic and potential energies and simplify the budgets in § 4.3. Finally, we focus on one particular simplified budget in order to formulate an hypothesis regarding the regime transitions in § 4.4.

4.1. *Local energy budgets*

The governing equations on which all subsequent analyses are based are the incompressible Navier–Stokes equation under the Boussinesq approximation coupled to the advection–diffusion of density. Under the notation and conventions adopted in §§ 2.1–2.3, they take the following non-dimensional form:

$$\nabla \cdot \boldsymbol{u} = 0, \tag{4.1a}$$

$$\partial_t \boldsymbol{u} + \boldsymbol{u} \cdot \nabla \boldsymbol{u} = -\nabla p + Ri_B\,(-\cos\theta\,\hat{\boldsymbol{z}} + \sin\theta\,\hat{\boldsymbol{x}})\rho + \frac{1}{Re}\nabla^2 \boldsymbol{u}, \tag{4.1b}$$

$$\partial_t \rho + \boldsymbol{u} \boldsymbol{\cdot} \nabla \rho = \frac{1}{Re\, Sc} \nabla^2 \rho, \tag{4.1c}$$

where we recall that $Ri_B = 1/4$ and $Sc = 700$.

4.1.1. *Kinetic energy*

We first consider the kinetic energy field $\mathcal{K}$, defined as

$$\mathcal{K}(\boldsymbol{x}, t) \equiv \tfrac{1}{2} u_i u_i, \tag{4.2}$$

where, here and in the following, we adopt the summation convention over repeated indices. The evolution of $\mathcal{K}$ is obtained by the dot product of the momentum equation (4.1*b*) with $\boldsymbol{u}$. Using incompressibility (4.1*a*) and standard manipulations, we obtain

$$\frac{\partial \mathcal{K}}{\partial t} = \phi_{\mathcal{K}}^{adv} + \phi_{\mathcal{K}}^{pre} + \phi_{\mathcal{K}}^{vis} + \mathcal{B}_x - \mathcal{B}_z - \epsilon, \tag{4.3}$$

where the boundary fluxes due to advection $\phi_{\mathcal{K}}^{adv}$, pressure work $\phi_{\mathcal{K}}^{pre}$, viscous work $\phi_{\mathcal{K}}^{vis}$ are

$$\phi_{\mathcal{K}}^{adv} \equiv \frac{\partial}{\partial x_i}(-u_i \mathcal{K}), \quad \phi_{\mathcal{K}}^{pre} \equiv \frac{\partial}{\partial x_i}(-u_i p), \quad \phi_{\mathcal{K}}^{vis} \equiv \frac{2}{Re} \frac{\partial}{\partial x_j}(u_i s_{ij}), \tag{4.4a–c}$$

and where the volumetric horizontal buoyancy fluxes $\mathcal{B}_x$, vertical buoyancy flux $\mathcal{B}_z$ and viscous dissipation ϵ are

$$\mathcal{B}_x \equiv Ri_B \sin\theta\, \rho u, \quad \mathcal{B}_z \equiv Ri_B \cos\theta\, \rho w, \quad \epsilon \equiv \frac{2}{Re} s_{ij} s_{ij}. \tag{4.5a–c}$$

The symmetric strain rate tensor is $s_{ij} \equiv (\partial_{x_i} u_j + \partial_{x_j} u_i)/2$, and the dissipation rate is positive definite $\epsilon > 0$.

4.1.2. *Potential energy*

Next, we consider the potential energy field $\mathcal{P}$, defined as

$$\mathcal{P}(\boldsymbol{x}, t) \equiv Ri_B\, (z \cos\theta - x \sin\theta) \rho, \tag{4.6}$$

since the duct (x, y, z) coordinate system is tilted at angle θ with respect to the direction of gravity. The evolution of $\mathcal{P}$ is obtained by standard manipulations of the density conservation equation (4.1*c*) as

$$\frac{\partial \mathcal{P}}{\partial t} = \phi_{\mathcal{P}}^{adv} + \phi_{\mathcal{P}}^{dif} + \phi_{\mathcal{P}}^{int} - \mathcal{B}_x + \mathcal{B}_z, \tag{4.7}$$

where we recover the buoyancy fluxes $\mathcal{B}_x, \mathcal{B}_z$ defined in (4.5), and where the boundary fluxes of $\mathcal{P}$ due to advection $\phi_{\mathcal{P}}^{adv}$, diffusion $\phi_{\mathcal{P}}^{dif}$ and conversion of internal energy (heat) $\phi_{\mathcal{P}}^{int}$ are

$$\left.\begin{aligned} \phi_{\mathcal{P}}^{adv} &\equiv \frac{\partial}{\partial x_i}(-u_i \mathcal{P}), \\ \phi_{\mathcal{P}}^{dif} &\equiv \frac{Ri_B}{Re\, Sc} \frac{\partial}{\partial x_i} \left\{ (z \cos\theta - x \sin\theta) \frac{\partial \rho}{\partial x_i} \right\}, \\ \phi_{\mathcal{P}}^{int} &\equiv \frac{Ri_B}{Re\, Sc} \left\{ \cos\theta \frac{\partial \rho}{\partial z} - \sin\theta \frac{\partial \rho}{\partial x} \right\}. \end{aligned}\right\} \tag{4.8}$$

4.2. *Volume-averaged energy budgets*

We now consider the control volume V, a rectangular parallelepiped bounded by the four duct cross-sectional walls at $y, z = \pm 1$ of arbitrary non-dimensional length $\ell \in [0, 2A]$ centred around $\bar{x}$, i.e. $V = (x, y, z) \in [\bar{x} - \ell/2, \bar{x} + \ell/2] \times [-1, 1] \times [-1, 1]$ (V has a volume equal to $\ell \times 2 \times 2 = 4\ell$). When applied to our 3D-3C data, the control volume V will be the measurement volume shown in figure 1.

4.2.1. *Kinetic energy*

We define the volume-averaged kinetic energy K as

$$K(t) \equiv \langle \mathcal{K} \rangle_{x,y,z} \equiv \frac{1}{4\ell} \int_V \mathcal{K} \, \mathrm{d}V = \frac{1}{4\ell} \int_{-1}^{1} \int_{-1}^{1} \int_{\bar{x}-\ell/2}^{\bar{x}+\ell/2} \mathcal{K} \, \mathrm{d}x \, \mathrm{d}y \, \mathrm{d}z, \tag{4.9}$$

where, here and henceforth, $\langle \cdot \rangle_{x,y,z}$ denotes averaging over the control volume V.

We obtain the evolution equation of K by volume averaging (4.3). The volume-averaged boundary fluxes $\langle \Phi_{\mathcal{K}}^{adv} \rangle_{x,y,z}$, $\langle \Phi_{\mathcal{K}}^{pre} \rangle_{x,y,z}$, $\langle \Phi_{\mathcal{K}}^{vis} \rangle_{x,y,z}$ are simplified by the divergence theorem and the use of the no-slip boundary conditions $u_i = 0$ on the four solid duct boundaries $y, z = \pm 1$. All mean gradients along y and z therefore cancel, and the mean gradients along x take the general form $(1/\ell)\langle \cdot \rangle_{y,z}|_{L-R}$, where $\cdot|_{L-R}$ denotes the difference between the value of $\cdot$ on the left boundary of the volume (‘L’, $x = \bar{x} - \ell/2$) and its value on right boundary of the volume (‘R’, $x = \bar{x} + \ell/2$). We are left with

$$\frac{\mathrm{d}K}{\mathrm{d}t} = \Phi_K^{adv} + \Phi_K^{pre} + \Phi_K^{vis} + B_x - B_z - D, \tag{4.10}$$

where the boundary fluxes of K, the volume-averaged buoyancy fluxes and dissipation are, respectively,

$$\left.\begin{array}{l} \Phi_K^{adv} \equiv \dfrac{1}{\ell} \langle u\mathcal{K} \rangle_{y,z}|_{L-R}, \quad \Phi_K^{pre} \equiv \dfrac{1}{\ell} \langle up \rangle_{y,z}|_{L-R}, \quad \Phi_K^{vis} \equiv -\dfrac{1}{\ell} \dfrac{2}{Re} \langle u_i s_{i1} \rangle_{y,z}|_{L-R}, \\ \qquad B_x \equiv \langle \mathcal{B}_x \rangle_{x,y,z}, \quad B_z \equiv \langle \mathcal{B}_z \rangle_{x,y,z}, \quad D \equiv \langle \epsilon \rangle_{x,y,z}. \end{array}\right\} \tag{4.11}$$

4.2.2. *Potential energy*

We define the volume-averaged potential energy P by analogy with K as

$$P(t) \equiv \langle \mathcal{P} \rangle_{x,y,z} \equiv \frac{1}{4\ell} \int_V \mathcal{P} \, \mathrm{d}V = \frac{1}{4\ell} \int_{-1}^{1} \int_{-1}^{1} \int_{\bar{x}-\ell/2}^{\bar{x}+\ell/2} \mathcal{P} \, \mathrm{d}x \, \mathrm{d}y \, \mathrm{d}z. \tag{4.12}$$

By volume averaging (4.7) and using the no-slip boundary condition for velocity and no-flux boundary condition for density, we write the evolution of P as

$$\frac{\mathrm{d}P}{\mathrm{d}t} = \Phi_P^{adv} + \Phi_P^{dif} + \Phi_P^{int} - B_x + B_z, \tag{4.13}$$

where the boundary fluxes of P are

$$\Phi_P^{adv} \equiv Ri_B \frac{1}{\ell} (\cos\theta \, \langle z\rho u \rangle_{y,z}|_{L-R} - \sin\theta \, \langle x\rho u \rangle_{y,z}|_{L-R}), \tag{4.14a}$$

$$\Phi_P^{dif} \equiv \frac{Ri_B}{Re\,Sc} \frac{1}{\ell} \left(\sin\theta \, \left. \left\langle x \frac{\partial\rho}{\partial x} \right\rangle_{y,z} \right|_{L-R} - \cos\theta \, \left. \left\langle z \frac{\partial\rho}{\partial x} \right\rangle_{y,z} \right|_{L-R} \right), \tag{4.14b}$$

$$\Phi_P^{int} \equiv \frac{Ri_B}{Re\,Sc}\left(-\frac{1}{\ell}\sin\theta\langle\rho\rangle_{y,z}|_{L-R} + \frac{1}{2}\cos\theta\langle\rho\rangle_{x,y}|_{B-T}\right), \tag{4.14c}$$

where by analogy with $\cdot|_{L-R}$, we denote by $\cdot|_{B-T}$ the difference between the value of $\cdot$ at the bottom ('B', $z=-1$) and at the top ('T', $z=1$).

4.2.3. *Summary and schematics*

The evolution equations – or 'budgets' – for the volume-averaged kinetic energy K (see (4.10) and (4.11)) and potential energy P (see (4.13) and (4.14)) are summarised schematically in figure 5.

In addition to the kinetic energy K and potential energy P reservoirs, the fluid contained in the volume V has an internal energy (heat) reservoir I that we have hitherto not explicitly considered. As we shall see in § 4.3.2, we do not need to do so since the evolution of I is (to a very good approximation) slaved to that of K and does not feed back on either K or P.

These three reservoirs exchange energy via internal fluxes: K and P exchange energy with one another via *a priori* reversible (i.e. sign-indefinite) buoyancy fluxes B_x, B_z; K is irreversibly dissipated at a positive-definite rate $D>0$ to I; and I is irreversibly converted by molecular diffusion at a positive-definite rate $\Phi_P^{int}>0$ to P (this conversion does not necessitate macroscopic fluid motions). In addition, K, P and I also exchange energy via a number of boundary fluxes with the exterior (denoted by E). These boundary fluxes are all *a priori* reversible (i.e. sign indefinite). (Note that the boundary flux of I was not explicitly considered in the above discussion but it is necessary to close the I budget.)

The steady character of the sustained forcing in the SID experiment ensures that, when averaged over a sufficiently long time period, each energy reservoir must be in steady state. In other words, the time-averaged budgets are 'closed', in the sense that they all cancel,

$$\left\langle\frac{\mathrm{d}K}{\mathrm{d}t}\right\rangle_t \approx \left\langle\frac{\mathrm{d}P}{\mathrm{d}t}\right\rangle_t \approx \left\langle\frac{\mathrm{d}I}{\mathrm{d}t}\right\rangle_t \approx 0, \tag{4.15}$$

where $\langle\cdot\rangle_t \equiv (1/\tau)\int_0^\tau \cdot\,\mathrm{d}t$ denotes averaging over the recorded data (or 'duration of an experiment') τ. We expect this steady state (4.15) to be a very good approximation, certainly over periods of $O(10^2-10^3$ ATU) (the typical duration of an experiment), and presumably even over smaller periods of $O(10$ ATU) in the relatively steady L and H regimes.

These budgets are related to other energetic analyses applied to numerical simulations in the literature (see e.g. Winters *et al.* 1995, § 4), but have a number of features that make them unique to SID experiments: (i) the presence of a tilt angle $\theta>0°$ introducing the crucial horizontal buoyancy flux B_x; (ii) the presence of solid boundaries at $y, z=\pm 1$ cancelling the boundary fluxes along y and z; (iii) the absence of a periodic boundary condition in the x direction introducing non-zero boundary fluxes along x (contrary to most numerical simulations); and (iv) the asymptotic steadiness of all reservoirs due to the sustained forcing discussed above.

In the remainder of the paper, we make the approximation that

$$\cos\theta\approx 1 \quad \text{and} \quad \sin\theta\approx\theta, \tag{4.16a,b}$$

which is accurate to better than 0.5 % for the angles considered in this paper ($\theta\leqslant 6°$). Unless explicitly specified otherwise, θ will now be expressed in radians.

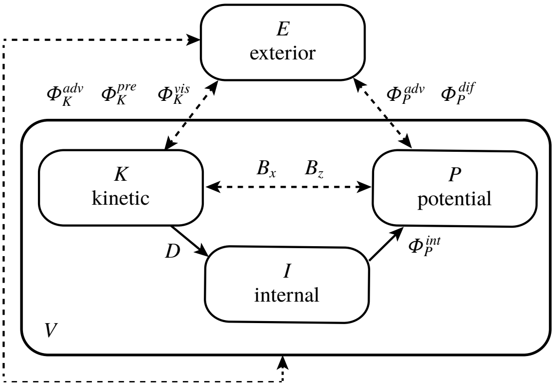

FIGURE 5. Schematics of the complete energy budgets in a control volume V. The V-averaged kinetic $K(t)$, potential $P(t)$ and internal $I(t)$ energy reservoirs exchange energy with one another via internal fluxes and with the exterior E via boundary fluxes. Solid arrows indicate irreversible (i.e. sign-definite) transfer, and dashed arrows indicate *a priori* reversible (i.e. sign-indefinite) transfer, until proven otherwise later. The *a priori* reversible transfer between E and I is acknowledged but was not explicitly derived in the text since it is not central to the discussion.

4.3. *Estimations and simplified budgets*

In this section we give physical interpretation of each of the fluxes relevant to SID flows in order to determine their sign, relative magnitude and, eventually, build a simplified picture of the time- and volume-averaged energetics of SID flows.

4.3.1. *The two-layer hydraulic model*

Consider the two-layer hydraulic model sketched in figure 6. The left (‘L’) boundary of the volume V (shaded in grey) has a lower layer velocity $u_{1L} > 0$, an upper layer velocity $u_{2L} < 0$, and the right (‘R’) boundary of V has a lower layer velocity $u_{1R} > 0$, and an upper layer velocity $u_{2R} < 0$. The position of the interface $\eta(x)$ (black solid curve) defined positive above the midplane $z = 0$ (black dashed line) takes the respective values of η_L and η_R at each boundary. In agreement with hydraulic theory, and to make the following calculations easier, we further assume a steady streamwise velocity profile uniform in each layer (i.e. depending only on x), and a hydrostatic pressure distribution where the reference pressure is 0 all along the interface $p(x, z = \eta(x)) = 0$ (after subtracting the hydrostatic streamwise pressure gradient due to $\theta \neq 0$). The local hydrostatic gradient is thus $\partial_z p = Ri_B\,\rho = (1/4)\rho$ (where in the lower layer $\rho_1 = 1$, in the upper layer $\rho_2 = -1$), giving a pressure distribution $p(x, z) = (1/4)\{\eta(x) - z\}$ (shown as thin black solid lines).

This flow has two distinct forcing mechanisms: (i) a horizontal hydrostatic pressure gradient of opposite sign in each layer, resulting from each end of the duct sitting in reservoirs containing fluids of different densities, which is present even when the duct is horizontal (i.e. when $\theta = 0°$); (ii) the gravitational acceleration of the buoyant layer to the left and the dense layer to the right at positive tilt angles $\theta > 0°$. To understand the relative importance of these forcing mechanisms, consider the

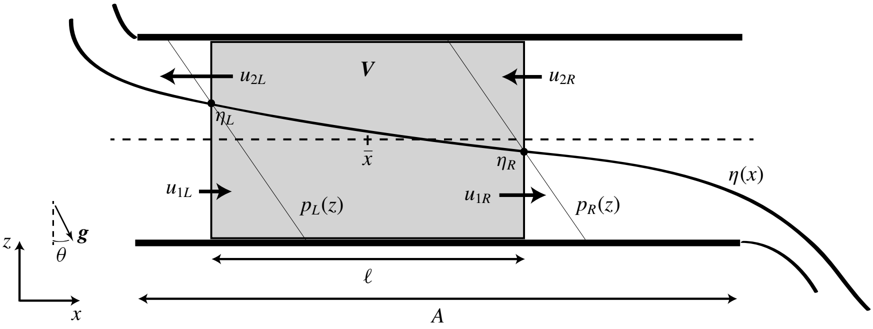

FIGURE 6. Schematics and notation used for the evaluation of boundary fluxes under hydraulic assumptions. The control volume V, centred on $\bar{x}$ and of length ℓ, is shaded in grey, and as before, 1 (respectively 2) denotes the lower (respectively upper) layer, and L (respectively R) denotes the left (respectively right) boundary of V. The interface has position $\eta(x)$ (solid curve) with respect to the neutral level $z=0$ (dashed). Note the hydrostatic pressure distributions $p_L(z)$ and $p_R(z)$ at the L and R boundaries (thin solid lines), with $p=0$ along the interface.

corresponding streamwise momentum equation (including viscous effects),

$$4\boldsymbol{u}\cdot\boldsymbol{\nabla}u=\underbrace{-\eta'(x)}_{\substack{hydrostatic\\ forcing}}+\underbrace{\theta\,\rho}_{\substack{gravitational\\ forcing}}+\frac{4}{Re}\nabla^2 u, \tag{4.17}$$

where $\rho(x,z)=\operatorname{sgn}(\eta(x)-z)=\pm 1$ by definition of $\eta(x)$. Since each layer convectively accelerates (and thus becomes thinner) in the direction in which is it flowing, the interface position η must be a monotonically decreasing function of x: $\eta'(x)<0$ for all x. Since in addition $\eta\in[-1,1]$, the average slope on the scale of the whole duct (taking $\ell=2A$) must be smaller than $2/2A=\alpha$, where we define the inverse aspect ratio of the duct as

$$\alpha\equiv A^{-1}. \tag{4.18}$$

We therefore have $\langle|\eta'(x)|\rangle_x<\alpha$, i.e. an upper bound on the magnitude of the average slope and, therefore, on the magnitude of the horizontal pressure gradient in (4.17). This bound holds for any sufficiently large volume V not centred in the immediate vicinity of the ends of the duct (where $|\eta'|$ may be large and the hydrostatic assumption may break down). Consequently, in such a control volume, a sufficient condition ensuring that the contribution of the gravitational forcing in (4.17) is always greater than the contribution of the hydrostatic forcing is that the tilt angle θ is 'large', which, in this paper, is understood relative to the 'geometrical' angle of the duct α, i.e.

$$\theta>\alpha. \tag{4.19}$$

For the duct discussed in this paper $\alpha=1/30\approx 2^\circ$. (Note that because of the length of the duct considered in this paper, a large tilt angle $\theta>2^\circ$ is still compatible with our approximation (4.16).)

A more accurate way to analyse the relative importance of the various terms in (4.17), including the viscous friction in $\nabla^2 u$, is through the framework of frictional two-layer hydraulic theory. Originally proposed by Schijf & Schönfled (1953), and later formalised by Gu (2001), Gu & Lawrence (2005), this theory combines the hydraulic description of two-layer flows (see e.g. Armi (1986)) with frictional stresses at solid boundaries and at the interface created by the inevitable (y, z) dependence of the underlying velocity profiles. By parameterising the local loss of streamwise momentum due to these stresses by the local uniform model velocities $u_1(x)$, $u_2(x)$ using a small number of non-dimensional friction parameters, an expression for the local slope of the interface $\eta(x)$ can be derived. An adaptation of this theory for non-zero tilt angles $\theta \neq 0$ can be found in L18, Chap. 5 but falls outside the scope of this paper. Here we limit ourselves to discussing the simple result that at the middle point $(x = 0)$ of a tilted duct the interfacial slope is proportional to

$$\eta'(0) \propto \theta - F, \tag{4.20}$$

where F is the so-called 'friction slope', a complicated expression combining wall and interfacial stress parameters. The above equation can be interpreted as follows: the viscous frictional stresses acting at the walls and at the interface parameterised in F tend to make the interface slope downwards (momentum sink), whereas the positive gravitational forcing $\theta > 0$ tends to make the interface slope upwards (momentum source). It follows that:

(i) When $0 < \theta \ll F$, viscous friction in the duct makes the interface slope downwards, but as discussed above, with a magnitude that cannot exceed the duct geometrical slope: $F < \alpha$. The friction F is largely independent of θ, which does not play a significant dynamical role. We call such flows lazy flows (figure 7*a*).

(ii) As θ is increased, the gravitational forcing makes the interface become increasingly horizontal (i.e. parallel to x) until it becomes nearly horizontal ($\eta'(0) \lesssim 0$) as θ approaches F from below. As θ is further increased above this initial value of F, the friction F must increase to follow θ very closely to enforce the necessary condition that the interface slopes downwards. This qualitative change in the behaviour of the friction F, now directly dependent on θ, must occur when $\theta > \alpha$ (since initially $F < \alpha$), yet it generally occurs for smaller θ (depending on the initial, unknown, value of F). In this situation, $F \gtrsim \theta$ and the interface is relatively flat throughout the duct ($\eta'(x) \lesssim 0$ for all x). We call such flows forced flows (figure 7*b*).

We believe that our distinction between lazy and forced flows is an important modelling result for the study of two-layer exchange flows forced by a positive angle $\theta > 0$. In the next section, we build on this distinction to derive a much-simplified budget.

4.3.2. *Simplified budgets*

Based on the simplified two-layer hydraulic model introduced above, we derived estimations of each term of the full energy budget (4.11), (4.14) in appendix B.

A first level of simplification of the full budget presented in figure 5 consists in neglecting the boundary fluxes Φ_K^{pre}, Φ_K^{vis}, Φ_P^{dif} and Φ_P^{int} for the Re and Sc considered in this paper (as argued in appendix B). The resulting simplified budget for lazy flows is sketched in figure 8(*a*), in which all the energy in V is supplied by the

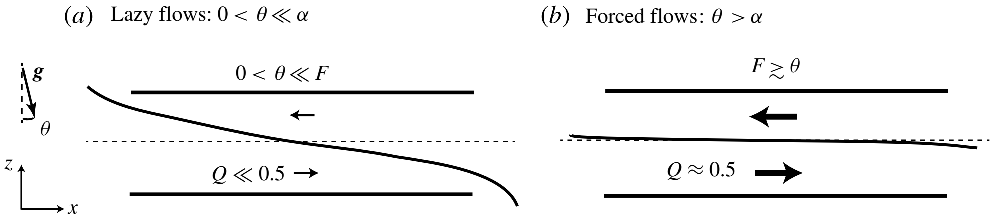

FIGURE 7. Qualitative distinction based on frictional hydraulic theory between (*a*) 'lazy' flows (at small tilt angles θ), in which viscous effects in F dominate over the gravitational forcing by θ; and (*b*) 'forced' flows (at large tilt angles θ) in which both effects are in balance, leading to a relatively flat interface throughout the duct and $Q \approx 0.5$.

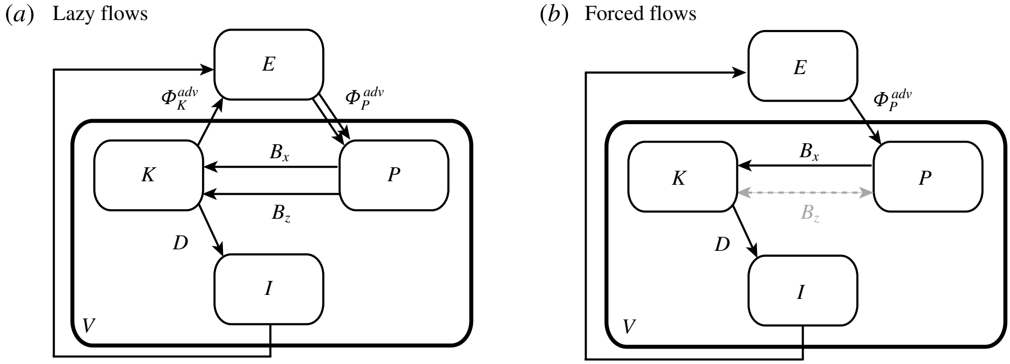

FIGURE 8. Schematics of two simplified energy budgets. The energy fluxes in the general budget of figure 5 were estimated in appendix B using the two-layer hydraulic model of figure 6, and led to two levels of simplifications for (*a*) lazy flows and (*b*) forced flows.

positive advective flux of P ($\Phi_P^{adv} > 0$) composed of hydrostatic and gravitational contributions (represented by a double arrow). This energy is transferred to K by the horizontal buoyancy flux ($B_x > 0$), equal to the gravitational contribution of Φ_P^{adv}. We previously argued that the vertical buoyancy flux B_z was, in general, sign indefinite, depending on the level of vertical motions in the flow. However it now becomes clear that, in order to close the budgets of lazy flows over sufficiently long times, B_z must be a sink to P and a source to K ($B_z < 0$), and it must equal the hydrostatic contribution of Φ_P^{adv} in magnitude. To balance these two distinct sources, K has two distinct sinks: the advective flux $\Phi_K^{adv} < 0$, and the viscous dissipation $-D < 0$. The internal energy reservoir I has an energy source $D > 0$, which in steady state, is balanced by a negative advective boundary flux to E.

A second level of simplification is possible in the special case of forced flows, as sketched in figure 8(*b*). We show in appendix B that in a 'periodic' volume V (expected when $\theta > \alpha$) the hydrostatic contribution of the source term Φ_P^{adv} and the advective flux Φ_K^{adv} both cancel. The budget becomes very simple: to a good approximation, the main source of P is $\Phi_P^{adv} = (Q_m/4)\theta$, which corresponds exactly to its main sink (and therefore the main source of K) $B_x = \Phi_P^{adv} = (Q_m/4)\theta$. Therefore, although B_z is truly sign indefinite in this case and may be responsible for unsteady reversible energy transfers on short time scales, its temporal average must cancel and become irrelevant in steady state over the duration of an experiment (hence we represent it by a grey dashed arrow). We thus conclude that for forced flows in steady state P, K (and I) all have only a single source and a single sink, which must all be equal in magnitude,

$$\langle \Phi_P^{adv} \rangle_t = \langle B_x \rangle_t = \langle D \rangle_t = \tfrac{1}{4} \langle Q_m \rangle_t \theta. \tag{4.21}$$

This is one of the main modelling results of this paper. It states that the time- and volume-averaged energetics of forced flows in any control volume of the SID is reducible to a single flux which depends only on the magnitude of the mass flux exchanged between the two reservoirs $\langle Q_m \rangle_t$, and the tilt angle of the duct θ.

Another very attractive feature of forced flows is that the energy budgets we derived are valid in any control volume V in the duct regardless of its location $\bar{x}$ and length ℓ. This is true as long as V is not located in the immediate vicinity of the ends of the duct ($x = \pm A$) where the hydrostatic approximation is questionable and as long as V is sufficiently long (say $\ell \gg 1$) for the volume-averaging to make sense. Thus, by virtue of the x-periodicity of forced flows, the volume-averaged energetics of the whole duct are equal to that of any of its sub-volume and, in particular, of any sensible 3D-3C measurement volume.

4.4. *Implications: hypothesis for regime transitions*

We now propose that the volume-averaged square norm of the (non-dimensional) strain rate tensor S, defined as

$$S \equiv \langle \mathsf{s}_{ij} \mathsf{s}_{ij} \rangle_{x,y,z} = \frac{Re}{2} D, \tag{4.22}$$

is a good candidate for a quantitative proxy of the flow regimes (as opposed to the viscous dissipation D because of its $Re/2$ factor). In the remainder of the paper, we primarily focus on S and refer to it as 'viscous dissipation' for simplicity (which is the correct standard terminology with respect to the rescaled time coordinate $t^* \equiv t/(Re/2)$). Since the hydraulic controls at both ends of the duct limit the mean value of streamwise motions to $|u|_{x,y,z} = Q \lesssim 0.5$ and vertical motion must realistically be even smaller, we expect the range of spatial scales over which the strain rates act in V to be the main variable of adjustment between flow regimes. We thus expect laminar flows with gradients over lengths of $O(1)$ to have $S = O(1)$ and increasingly turbulent flows with increasingly small-scale motions to have much larger gradients and $S \gg 1$.

It therefore appears natural to propose that the L, H, I, T regimes correspond to increasingly large values of the time-averaged dissipation $\langle S \rangle_t$. This intuitive idea can be formalised using the regime function (see (2.11)) as the following simple hypothesis:

$$\mathrm{reg} = \mathrm{reg}(\langle S \rangle_t), \tag{4.23}$$

where reg is a monotonically increasing function of $\langle S \rangle_t$ only. This hypothesis is general and does not assume that the flow is lazy or forced.

Our main modelling result (4.21) that the time- and volume-averaged dissipation $\langle S \rangle_t$ in forced flows can be predicted from the knowledge of θ, Re (input parameters) and Q_m (output parameter) can be rewritten as

$$\langle S \rangle_t = \frac{Re}{2} \langle D \rangle_t = \frac{1}{8} \langle Q_m \rangle_t \theta Re. \tag{4.24}$$

Despite Q_m being an output parameter, frictional hydraulic theory and extensive empirical evidence (see ML14, L18 § 3.6 and figure 9 below) suggest that the hydraulic limit of $Q_m \approx 0.5$ is usually a good approximation in forced flows, so long as they are not excessively turbulent, since excessive turbulence and mixing acts to reduce Q_m for very high values of θ and Re (as will be shown in figure 9 below).

Therefore, the corollary of hypothesis (4.23) in the special case of forced flows is that regime transitions follow the simple scaling

$$\langle S \rangle_t \approx \tfrac{1}{16}\,\theta Re, \tag{4.25}$$

and (4.23) can be recast in terms of input parameters only

$$\mathrm{reg} = \mathrm{reg}(\theta Re), \tag{4.26}$$

where reg is a monotonically increasing function of θRe only.

In the next section, we discuss experimental data to examine the hypothesis (4.23) and its corollary (4.26).

5. Experimental validation

In this section, we examine whether or not regime transitions:

(i) indeed scale with the non-dimensional group of parameters θRe (the forced flow corollary of our physical hypothesis) using our regime data in § 5.1;

(ii) are indeed caused by increasing values of the time- and volume-averaged dissipation $\langle S \rangle_t$ (our underlying physical hypothesis) using our 3D-3C data in §§ 5.2–5.3.

5.1. *Observed regime transitions scaling*

To compare the scaling of the transitions in our experimental data with the model and predictions of the previous sections, we plot in figure 9 four distinct types of data in the θ–Re plane:

(i) The flow regime data of figure 2 using the same symbols (note that θ is expressed in radians here using a log scale, restricting us to $\theta > 0$ data).

(ii) Two families of thick lines indicating two distinct scaling: the dotted lines have slope $-1/2$ and indicate a power law scaling of the form $\theta Re^2 = \text{const.}$ while the dashed lines have slope -1 and indicate a power law scaling of the form $\theta Re = \text{const.}$ These were set manually in order to best fit the data.

(iii) A vertical grey shading at $\theta = \alpha$ representing the upper bound for the expected boundary between lazy flows and forced flows (see § 4.3.1).

(iv) Thin black contours showing a fit of $\langle Q_m \rangle_t$ based on averaged mass flux measurements that were carried out for a subset of experiments (161 in total) using salt mass balances as in ML14 (note the equivalence between our definition and their 'Froude number' $F \equiv \sqrt{2}\langle Q_m \rangle_t$). For more details on the salt mass balance method see Lefauve 2018, § 2.2. These data were then fitted by least-squares assuming a quadratic form in the $(\log\theta, \log Re)$ plane.

We make the following observations:

(i) The mass flux data $\langle Q_m \rangle_t$ are best fitted by a quadratic form describing hyperbolas having a major axis of slope -0.67, i.e. an equation $\theta Re^{3/2} = \text{const.}$

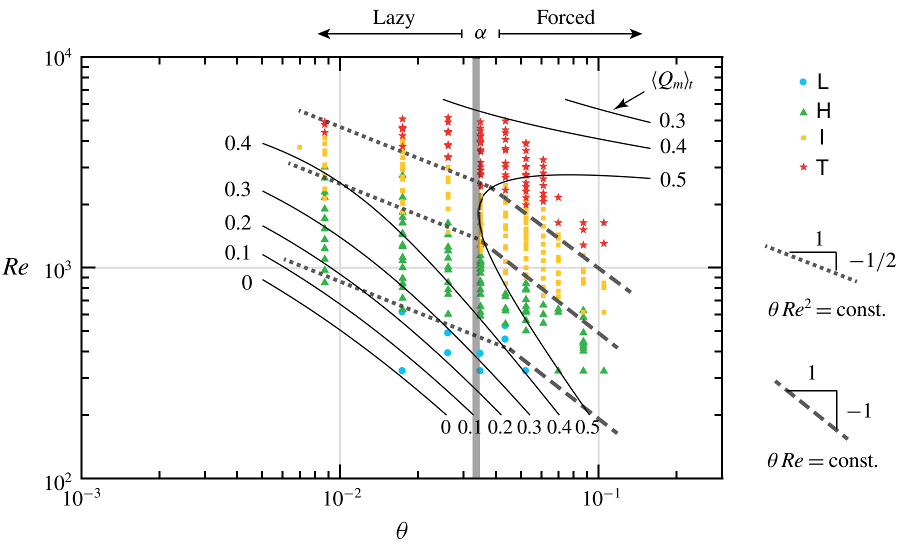

FIGURE 9. (Colour online) Experimental data on the scaling of regime transitions. The colour symbols are identical to figure 2, and are plotted in the same θ–Re plane, but with θ in radians (also note the log–log scale, restricting us to $\theta > 0$). The families of thick dotted and dashed lines represent approximate regime transition lines with respective scalings $\theta\, Re^2 = \text{const.}$ and $\theta Re = \text{const.}$ The vertical grey shading at $\theta = \alpha$ is the boundary between lazy and forced flows. The thin solid black contours are the quadratic form fitting of 161 mass flux measurements of $\langle Q_m \rangle_t$. Six contours are shown in the range 0–0.5 and they have been continued beyond the range covered by the data points used (note that no 0.6 contour exists here).

This empirical scaling, and more generally, the function $\langle Q_m \rangle_t(\theta,\ Re)$, are not presently understood and fall outside the scope of the present study (see L18, § 3.6 for more details). Here, we limit ourselves to the empirical observations that: (i) for the 'lazy' data ($\theta < \alpha$), as θ and Re increases, $\langle Q_m \rangle_t$ increases from $\ll 0.5$ (L regime) to ≈ 0.5 (I and T regimes); (ii) for the 'forced' data ($\theta > \alpha$), $\langle Q_m \rangle_t \approx 0.5$. These two observations, given the fact that $Q_m \approx Q$ (except for the most turbulent data), are consistent with the theoretical predictions of § 4.3.1.

(ii) In lazy flows, the regime data follow a reg $\sim \theta\, Re^2$ scaling (dotted lines). The L $\rightarrow$ H, H $\rightarrow$ I, and I $\rightarrow$ T transitions curves are respectively $\theta\, Re^2 = 6 \times 10^3,\ 6 \times 10^4,\ 2 \times 10^5$. This empirical 'lazy flow scaling' is not consistent with the theoretical 'forced flow scaling' predicted by the corollary (4.26), which is not surprising given the different energetics of lazy flows. This θRe^2 scaling is however consistent with the scaling proposed by ML14 (see § 2.4 and (2.9)), but this may be a coincidence that is not presently understood.

(iii) In forced flows, the regime data follow a reg $\sim \theta\, Re$ scaling (dashed lines). The L $\rightarrow$ H, H $\rightarrow$ I, and I $\rightarrow$ T transitions are respectively $\theta\, Re \approx 20,\ 50,\ 100$. This empirical 'forced flow scaling' is consistent with the corollary (4.26) (and inconsistent with ML14).

We have thus confirmed one of the features underlying the distinction between lazy and forced flows ($Q \approx Q_m < 0.5$ versus ≈ 0.5, respectively), as well as the regime

Name	θ (deg.)	Re	θRe	Volume properties			Resolution of data		
				$\bar{x}$	ℓ	τ	Δx, Δz	Δy	Δt
L1	2	398	14	−12.2	10.4	936	0.026	0.061	3.75
H1	1	1455	25	−12.2	10.4	459	0.025	0.053	2.29
H2	5	402	35	−11.9	10.8	302	0.025	0.074	1.03
H3	2	1059	37	−12.4	11.2	351	0.025	0.036	2.64
H4	5	438	38	−12.0	11.0	335	0.027	0.069	1.08
I1	2	1466	51	−12.4	11.2	508	0.026	0.036	3.65
I2	2	1796	63	−12.4	11.1	456	0.025	0.061	2.90
I3	2	2024	71	−12.5	11.1	722	0.025	0.063	3.28
I4	6	777	81	−12.6	7.73	248	0.019	0.057	1.65
I5	5	956	83	−11.0	10.0	332	0.025	0.067	1.27
I6	6	798	83	−12.6	7.67	116	0.019	0.059	0.85
I7	3	1580	83	−14.0	7.49	223	0.018	0.056	1.68
I8	5	970	84	−11.9	11.8	250	0.026	0.054	1.69
T1	3	2331	122	−14.0	7.50	407	0.019	0.057	2.70
T2	6	1256	131	−12.5	7.66	203	0.019	0.057	1.34
T3	5	1516	132	−11.9	11.1	554	0.025	0.053	2.39

TABLE 2. List of the 16 3D-3C experiments used, showing the input parameters θ and Re, volume properties and resolution of data. In the second column only, θ is expressed in (deg.). Experiments are sorted by increasing θRe.

transitions scaling in forced flows reg = reg(θRe) (corollary (4.26)), but showed that lazy flows followed a different (and still unexplained) scaling.

In order to confirm the hypothesis (4.23) underlying the corollary, and thus to provide a physical basis for our understanding of regime transitions, we need to validate the energetics framework of § 4, and in particular, we need direct evidence that the energy budget of forced flows indeed follows the simplified model in figure 8(*b*). This is the subject of the next section.

5.2. *Experimental energy budgets*

We turn our attention to the energy budgets of 16 3D-3C experiments, whose input parameters, volume properties and resolution are detailed in table 2. They include one experiment in the L regime ($\theta\, Re < 20$, named 'L1'), four in the H regime ($20 < \theta\, Re < 50$, 'H1' to 'H4'), eight in the I regime ($50 < \theta\, Re < 100$, 'I1' to 'I8') and three in the T regime ($\theta\, Re > 100$, 'T1'to 'T3').

In figure 10, we plot the five main time-averaged energy fluxes of interest to validate the energetics model of § 4 and figure 8: $\langle \Phi_P^{adv} \rangle_t$ (magenta triangles), $\langle \Phi_K^{adv} \rangle_t$ (orange triangles), $\langle B_x \rangle_t$ (black line and squares), $\langle B_z \rangle_t$ (green lozenges) and $\langle D \rangle_t$ (blue stars). In this plot, the vertical coordinate of each symbol represents the value of its respective flux, and its horizontal coordinate represents the value of the horizontal buoyancy flux $\langle B_x \rangle_t$ for this particular experiment. All fluxes are therefore effectively plotted against $\langle B_x \rangle_t$, whose definition $\langle B_x \rangle_t = (1/4)\langle Q_m \rangle_t \theta \approx \theta/8$ (assuming $Q_m \approx 0.5$) makes it closest to being an input parameter. Note that this choice of horizontal coordinate automatically groups the data by increasing values of θ (i.e. importantly not by increasing $\theta\, Re$, thus not by regime). Note that the $\theta = 2^\circ$ group of data

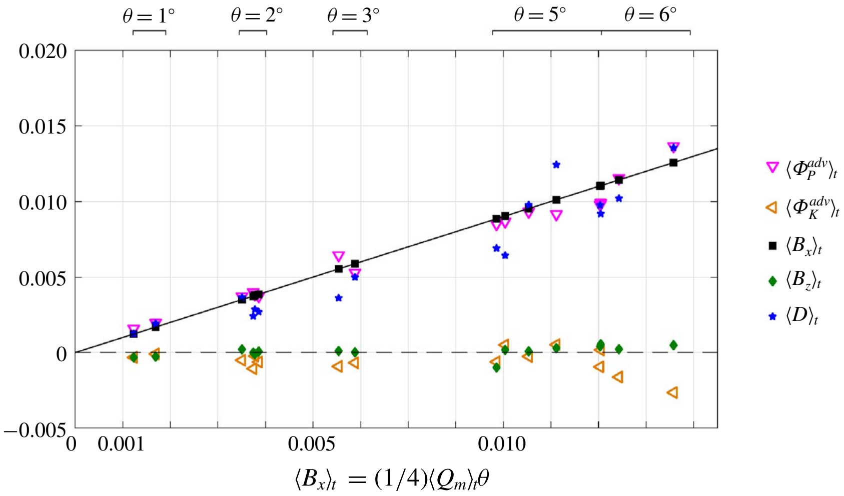

FIGURE 10. (Colour online) Experimental validation of the simple 'forced flow' energetics model sketched in figure 8(*b*). Time-averaged energetics of the 16 3D-3C experiments in table 2. Each flux retained in the general 'lazy flow' model of figure 8(*a*) was calculated using (4.11) and (4.14) and is plotted against $\langle B_x \rangle_t$ (close to being the input parameter θ), showing that, as expected for forced flows, $\langle \Phi_P^{adv} \rangle_t \approx \langle B_x \rangle_t \approx \langle D \rangle_t$ and $\langle \Phi_K^{adv} \rangle_t \approx \langle B_z \rangle_t \approx 0$.

includes a mix of L, H and I flows, the $\theta = 5°$ group includes H, I and T flows and the $\theta = 3°$ and $\theta = 6°$ groups include I and T flows.

We observe that $\langle \Phi_P^{adv} \rangle_t$ (main source of P) and $\langle D \rangle_t$ (main sink of K) closely follow the buoyancy flux $\langle B_x \rangle_t$ ($P \rightarrow K$ exchange) at all angles. The dissipation data show the greatest discrepancy (i.e. the blue stars lie further away from the black line and squares than the magenta triangles do) as we will explain in § 5.3. We also verify that the advective flux of kinetic energy and the vertical buoyancy fluxes, which are only expected to be relevant in lazy flows, are indeed close to zero: $\langle \Phi_K^{adv} \rangle_t$, $\langle B_z \rangle_t \approx 0$ (see dashed line).

In other words, the simplified budgets of figure 8(*b*) for forced flows and our main prediction (4.21) that the energetics of SID flows are reducible to a single energy flux (that we may refer to as 'power throughput') appear to be good approximations for $\theta \in [1°, 6°]$, that is, even when the necessary condition for forced flows $\theta > \alpha \approx 2°$ does not hold.

Although we do not show the results, we verified that the experimental time-averaged kinetic and potential energy budgets do indeed cancel to an excellent approximation: $\langle \mathrm{d}P/\mathrm{d}t \rangle_t \approx \langle \mathrm{d}K/\mathrm{d}t \rangle_t \approx 0$ as hypothesised in (4.15) (the flow has steady P and K reservoirs). However, it is clear from figure 10 that, for some experiments, these budgets do not cancel to such a good approximation when indirectly computed from the sum of experimentally determined fluxes (i.e. $\langle \mathrm{d}P/\mathrm{d}t \rangle_t = \langle \Phi_P^{adv} \rangle_t - \langle B_x \rangle_t + \langle B_z \rangle_t$ and similarly $\langle \mathrm{d}K/\mathrm{d}t \rangle_t = \langle \Phi_K^{adv} \rangle_t + \langle B_x \rangle_t - \langle B_z \rangle_t - \langle D \rangle_t$ as per figure 8). This is due to the greater experimental errors in determining boundary fluxes and dissipation rates than in determining $\mathrm{d}K/\mathrm{d}t$ and $\mathrm{d}P/\mathrm{d}t$ directly, as expected from the nature of the experimental data.

In figure 11, we re-plot the buoyancy flux and dissipation data of figure 10 (black squares and blue stars) rescaled by $Re/2$. The dissipation $\langle S \rangle_t = (Re/2)\langle D \rangle_t$ is our hypothetical proxy for the flow regimes and we test its dependence on the transition

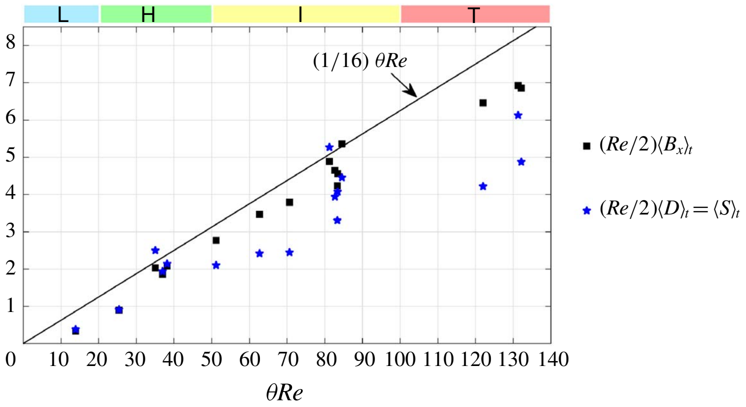

FIGURE 11. (Colour online) Dissipation and buoyancy flux data of figure 10 (same symbols) rescaled by $Re/2$ and plotted against the input parameter θRe to test the corollary (4.25) (black line).

parameter θRe expected from the corollary (4.26). Plotted against this horizontal axis, the data are no longer grouped by angles (as was the case in figure 10); rather they are grouped by increasing flow regimes (as shown by the coloured boxes at the top of the figure).

These data generally support the physical hypothesis that each flow regime corresponds to a well-defined range of $\langle S\rangle_t$ scaling with θRe. However, the agreement with the simplified scaling (4.25) $\langle S\rangle_t \approx (1/16)\theta Re$ (black solid line) is not particularly impressive (blue stars lying below the black line in all but two experiments), and gets worse as the flow gets increasingly more turbulent. This discrepancy has two causes: (i) the approximation $\langle Q_m\rangle_t = 0.5$ is an upper bound for most experiments (black squares lying below the black line) as discussed in §§ 3.2 and 5.1; (ii) the viscous dissipation is generally underestimated in experiments (blue stars lying below the black squares). We discuss the latter next.

5.3. *Experimental limitations in measuring the dissipation*

The previous section showed that, despite measurements showing that the kinetic energy reservoir was steady $(Re/2)\langle \mathrm{d}K/\mathrm{d}t\rangle_t \approx 0$, its sink $\langle S\rangle_t$ was generally measured to be smaller in magnitude than its source $(Re/2)\langle B_x\rangle_t$ in the I and T regimes. This is due to at least three experimental limitations specific to measurements of the dissipation:

First, numerically, the dissipation is the only flux that requires computation of flow field derivatives. Despite our use of a second-order accurate finite-difference scheme to compute the components of the strain rate tensor, experimental errors are bound to be amplified by differentiation especially in the I and T regimes where gradients are computed over small length scales;

Second, dynamically, measurements of turbulent dissipation rates require a fine enough spatial resolution, i.e. a grid size $(\Delta x, \Delta y, \Delta z)$ small enough to capture the smallest dynamically active scale. It is generally acknowledged that the spectral content of dissipation becomes negligible below the Kolmogorov length scale, which is defined dimensionally as $L_k \equiv (\nu^3/\langle\epsilon\rangle_{x,y,z,t})^{1/4}$ (where, here and here only, L_k and ϵ are dimensional). Because we know that the kinetic energy budget is closed, we

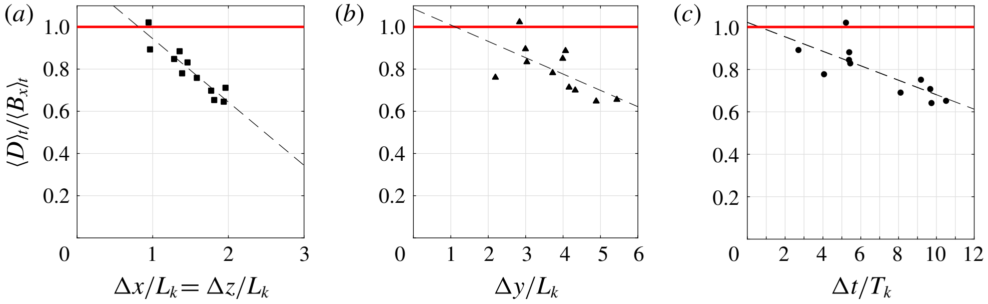

FIGURE 12. (Colour online) Effect of the spatio-temporal resolution of experiments on the accuracy of dissipation measurements in the I and T experiments of table 2 and figures 10–11. Measurements converge towards the expected value ($\langle D\rangle_t = \langle B_x\rangle_t$, red line) for increased (a,b) spatial resolution and (c) temporal resolutions (better 'freezing' of volumes), with respect to the Kolmogorov length and time scale, respectively. Dashed line represents the best linear fit. Note the different x-axis limits between the three panels.

use the estimated time- and volume-averaged dissipation of our corollary (4.25) to estimate the non-dimensional Kolmogorov length scale as

$$L_k \equiv \frac{1}{(H/2)}\left[\frac{\nu^3}{2\nu\dfrac{g'H}{(H/2)^2}\langle s_{ij}s_{ij}\rangle_{x,y,z,t}}\right]^{1/4} \approx 2^{3/4}(\theta Re^3)^{-1/4}. \tag{5.1}$$

For each of the 11 experiments in the I and T regimes, we plot in figure 12(a,b) the ratio $\langle B_x\rangle_t/\langle D\rangle_t$ against the spatial resolution normalised by the Kolmogorov length scale (5.1): $\Delta x/L_k = \Delta z/L_k$ in panel (a) and $\Delta y/L_k$ in panel (b). We observe that the estimates of dissipation become more accurate (converging to the red horizontal line) as the spatial resolution approaches the Kolmogorov length scale (the dashed line is the best linear fit to the data and intercepts the red line at Δx, $\Delta z \approx L_k$). In other words, experiments featuring the largest discrepancy in figure 11 were the ones in which the spatial resolution of experimental measurements was not sufficient given the level of turbulence expected for their value of θRe. We note that this trend was not observed when the data were plotted against Δx, Δy, Δz alone (i.e. the Kolmogorov scale is important). This latter observation suggests that the lack of spatial resolution dominates over the numerical inaccuracies associated with derivatives discussed in the previous paragraph.

Third, accurate measurements of flow gradients require our 3D-3C measurements to be as instantaneous as possible. As discussed in § 3.1 and appendix A, our scanning technique sets a lower bound on the non-dimensional time resolution Δt over which a volume is constructed. These non-instantaneous measurements inevitably distort turbulent flow structures. Figure 12(c) quantifies this impact and demonstrates that better temporal resolutions with respect to the non-dimensional Kolmogorov time scale $T_k \equiv 2^{3/2}(\theta Re)^{-1/2}$ (estimated similarly to (5.1)), in other words better 'freezing' of the volumes, result in better estimates of $\langle S\rangle_t$ (the fit intercepts the red line for perfect freezing at $\Delta t/T_k \approx 0$, as expected). The reason why such distortions lead to under-estimations (as opposed to over-estimations) of velocity gradients is still poorly understood.

6. Regimes and three-dimensionality

In the previous section, we validated experimentally our hypothesis that regime transitions correlate with an increase in the non-dimensional, volume-averaged strain rate S (that we refer to as 'dissipation') and our corollary that they both scale with θRe.

In this section, we investigate the link between flow energetics and three-dimensionality. We start by analysing the energy budgets of forced flows in more detail by subdividing the kinetic energy into a two-dimensional and a three-dimensional part in § 6.1, before sketching them and discussing their implications for regime transitions in § 6.2. We then validate this framework using experimental data in § 6.3 and focus on spatial structures in § 6.4.

6.1. *Two-dimensional and three-dimensional kinetic energy budgets*

We start by defining, for any flow field ϕ, a decomposition into a streamwise-averaged two-dimensional component ϕ^{2d} and a complementary three-dimensional component ϕ^{3d}:

$$\phi(x, y, z, t) = \phi^{2d}(y, z, t) + \phi^{3d}(x, y, z, t), \tag{6.1}$$

where

$$\phi^{2d}(y, z, t) \equiv \langle \phi \rangle_x, \tag{6.2a}$$

$$\phi^{3d}(x, y, z, t) \equiv \phi - \langle \phi \rangle_x. \tag{6.2b}$$

This decomposition is inspired from similar decompositions applied to direct numerical simulations (DNS) of stratified turbulence initiated by secondary instabilities developing on Kelvin–Helmholtz (KH) billows (Caulfield & Peltier 2000; Peltier & Caulfield 2003; Mashayek & Peltier 2012*a*,*b*; Mashayek, Caulfield & Peltier 2013; Salehipour, Peltier & Mashayek 2015). These studies typically decomposed the kinetic energy and associated fluxes into a one-dimensional part, corresponding to an initial base flow varying along z, a two-dimensional (x, z) part corresponding to coherent structures resulting from a primary KH instability and a three-dimensional (x, y, z) part corresponding to inherently turbulent structures. Our decomposition is slightly different in order to reflect the fact that, due to confinement by the duct boundaries, the SID 'base flow' is an inherent two-dimensional function of y and z (for more details see LPZCDL18 § 5.3).

Next, we define the volume-averaged two- and three-dimensional kinetic energies based on the respective velocity fields:

$$K^{2d}(t) \equiv \langle \mathcal{K}^{2d} \rangle_{y,z} \equiv \tfrac{1}{2} \langle u_i^{2d} u_i^{2d} \rangle_{y,z}, \tag{6.3a}$$

$$K^{3d}(t) \equiv \langle \mathcal{K}^{3d} \rangle_{x,y,z} \equiv \tfrac{1}{2} \langle u_i^{3d} u_i^{3d} \rangle_{x,y,z}. \tag{6.3b}$$

Importantly, we verify that the total kinetic energy is the sum of both components: $K = K^{2d} + K^{3d}$, since $\langle \mathcal{K} \rangle_x = \langle \mathcal{K}^{2d} \rangle_x + \langle \mathcal{K}^{3d} \rangle_x + u_i^{2d} \langle u_i^{3d} \rangle_x$ and $\langle u_i^{3d} \rangle_x = 0$ by definition. In order to write the evolution of $\mathcal{K}^{2d}$ and K^{2d}, we first x-average the momentum equation, which involves a number of gradients and divergence terms of the form

$$\left\langle \frac{\partial \phi}{\partial x_i} \right\rangle_x = \underbrace{\left\langle \frac{\partial \phi}{\partial x} \right\rangle_x}_{mean\ \ gradient} + \frac{\partial \langle \phi \rangle_x}{\partial x_i}. \tag{6.4}$$

In this integration by parts, ϕ may represent $u_i u_j$ (convective term), p (pressure gradient) or u_i (diffusive term). At this point, the assumption of periodic boundaries in x, consistent with forced flows (see figure 7*b*), becomes essential in order to cancel all mean gradients along x (the first term on the right-hand side) and make analytical progress (by avoiding very lengthy expressions). Thus, under this essential periodic assumption, we derive the following simple budgets:

$$\frac{\mathrm{d}K^{2d}}{\mathrm{d}t^*} = \frac{Re}{2}\frac{\mathrm{d}K^{2d}}{\mathrm{d}t} = \frac{Re}{2}(B_x^{2d} - B_z^{2d}) - S^{2d} - T, \tag{6.5a}$$

$$\frac{\mathrm{d}K^{3d}}{\mathrm{d}t^*} = \frac{Re}{2}\frac{\mathrm{d}K^{3d}}{\mathrm{d}t} = \frac{Re}{2}(B_x^{3d} - B_z^{3d}) - S^{3d} + T, \tag{6.5b}$$

where the rescaled 'fast' time $t^* \equiv t/(Re/2)$, previously introduced in § 4.4, is now used to facilitate general comparison between all experiments (making the horizontal buoyancy flux scale with θRe and the rate of viscous dissipation be S instead of D). We define the above two-dimensional and three-dimensional buoyancy fluxes, dissipation, and the new transfer term T between K^{2d} and K^{3d} as

$$B_x^{2d} \equiv \frac{\theta}{4}\langle \rho^{2d} u^{2d}\rangle_{y,z}, \quad B_z^{2d} \equiv \frac{1}{4}\langle \rho^{2d} w^{2d}\rangle_{y,z}, \quad S^{2d} \equiv \langle s_{2d}^2\rangle_{y,z}, \tag{6.6a}$$

$$B_x^{3d} \equiv \frac{\theta}{4}\langle \rho^{3d} u^{3d}\rangle_{x,y,z}, \quad B_z^{3d} \equiv \frac{1}{4}\langle \rho^{3d} w^{3d}\rangle_{x,y,z}, \quad S^{3d} \equiv \langle s_{3d}^2\rangle_{x,y,z}, \tag{6.6b}$$

$$T \equiv -\frac{Re}{2}\left\langle \langle u_i^{3d} u_j^{3d}\rangle_x \frac{\partial u_i^{2d}}{\partial x_j}\right\rangle_{y,z} \approx -\frac{Re}{2}\left\langle \langle u^{3d} w^{3d}\rangle_x \frac{\partial u^{2d}}{\partial z}\right\rangle_{y,z}. \tag{6.6c}$$

Although the transfer term T is defined as the sum of six terms (product of $i = 1, 2, 3$ by $j = 2, 3$), the approximation in (6.6*c*) reflects our observations that the single term $i = 1, j = 3$ represents over 90 % of the total in experiments (this is expected from the fact that turbulence is most active in the vicinity of the interface where the dominant shear is $\partial_z u^{2d}$).

6.2. *Sketch and implications for regime transitions*

A sketch of the time-averaged budgets in (6.3) is shown in figure 13 (using the fast t^* time scale), which improves on the sketch of figure 8(*b*). Note that we ignore the vertical buoyancy fluxes B_z^{2d}, B_z^{3d} as well as the three-dimensional horizontal buoyancy flux B_x^{3d} since they have been experimentally verified to be negligible (as expected). Panels (*a*) and (*b*) show fluxes of hypothetically different magnitudes under increasing 'power throughput' in the system $(Re/2)\langle \Phi_P^{adv}\rangle_t = (1/8)\langle Q_m\rangle_t \theta Re$ (represented by the thickness of the $E \rightarrow P$ arrow). Assuming $\langle Q_m\rangle_t \approx 0.5$, the time- and volume-averaged power throughput in the system is $\theta Re/16$, and we predict the following.

(i) For the lowest $\theta\, Re < 20$, the power throughput is $<20/16 = 1.25$, and $\langle S\rangle_t = \langle S^{2d}\rangle_t$ alone is sufficient to dissipate this power via the adjustment of the streamwise velocity profile $u(y, z)$ creating $O(1)$ gradients $|\partial_z u^{2d}|$ and $|\partial_y u^{2d}|$. This situation corresponds to the L regime, which, as we have seen in § 3.2, is essentially invariant in x.

(ii) For $20 < \theta Re < 50$, the power throughput is $1.25 < \langle S\rangle_t < 3.12$, and corresponds to the H regime, featuring the three-dimensional confined Holmboe waves (CHWs) described in LPZCDL18. To understand the L → H transition, we formulate two distinct hypotheses regarding the energetical importance of CHWs:

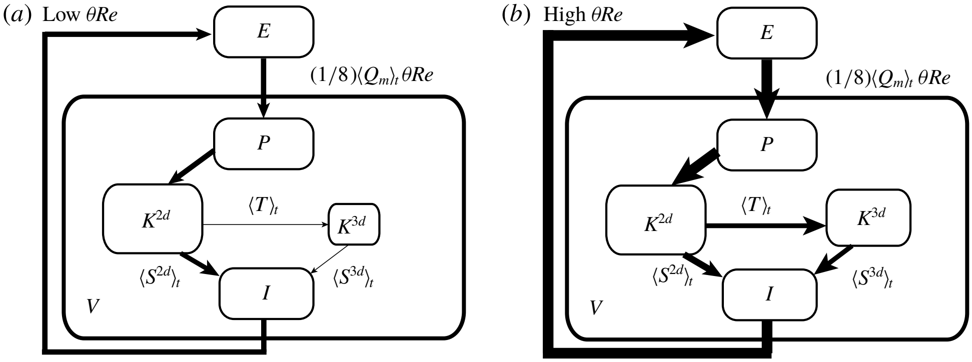

FIGURE 13. Energy budgets of forced flows using the $K = K^{2d} + K^{3d}$ decomposition, refining the budgets of figure 8(*b*). These budgets in (*a*) and (*b*) only differ in the hypothetical magnitude of the fluxes (with respect to the rescaled time t^*), represented by the thickness of the arrows: (*a*) at low θRe, the power throughput is small and dissipation by $\langle S^{2d}\rangle_t$ is sufficient; (*b*) at high θRe, the power throughput is high and transfer to K^{3d} by $\langle T\rangle_t$ and dissipation by $\langle S^{3d}\rangle_t$ takes over.

(1) HYP-1: the distortion of the two-dimensional flow u^{2d} to yield higher $\partial_z u^{2d}$, $\partial_y u^{2d}$ and $\langle S^{2d}\rangle_t$ 'incidentally' renders the flow profile u^{2d}, ρ^{2d} susceptible to the confined Holmboe instability (CHI) and triggers a transition to a weakly three-dimensional flow state, whose dissipation $\langle S^{3d}\rangle_t$ is insignificant (panel *a*). In other words additional dissipation is achieved primarily by u^{2d} and not by the three-dimensional CHWs, which are simply a by-product of the changes in u^{2d}.

(2) HYP-2: the distortion of u^{2d} is no longer sufficient to reach the target dissipation: no two-dimensional solutions exist with the required $\langle S^{2d}\rangle_t$ and the flow must 'bifurcate' to a three-dimensional state with significant transfer $\langle T\rangle_t$ and additional dissipation $\langle S\rangle_t \gg \langle S^{2d}\rangle_t$ (panel *b*). In other words additional dissipation is achieved by CHWs rather than by a continuing deformation of u^{2d}. This hypothesis was expressed in the last sentence of 'future direction (ii)' in LPZCDL18 (§ 7.2, p. 540) as a possible mechanism setting the amplitude of Holmboe waves.

Experimental data in the next section will allow us to decide which hypothesis is true.

(iii) For $\theta Re > 50$ (I regime), the power throughput becomes large >3.12 and we expect the transfer $\langle T\rangle_t$ and three-dimensional dissipation $\langle S^{3d}\rangle_t$ to be important to close the budgets (panel *b*). The H → I transition may be explained by two hypotheses which are respectively consistent with those above:

(1) HYP-1: if the CHW is energetically insignificant, its amplitude is presumably not influenced by θRe. Since it is the two-dimensional flow u^{2d} that responds to $\theta\,Re$, we expect the H → I transition to be related to an instability of this base flow.

(2) HYP-2: if the CHW is energetically significant in providing three-dimensional dissipation following $\theta\,Re$, its amplitude must be set by $\theta\,Re$ and we thus expect the H → I transition to be related to a 'secondary' instability of this wave state, perhaps due to a critical (nonlinear) amplitude.

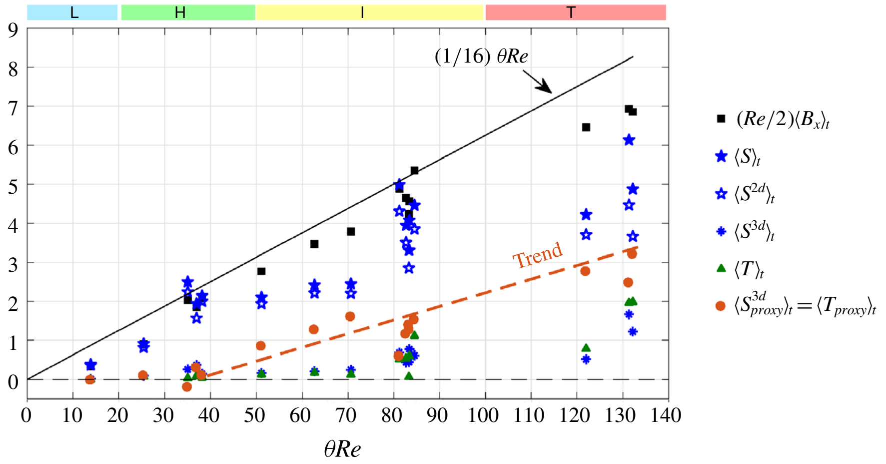

FIGURE 14. (Colour online) Experimental two-dimensional and three-dimensional kinetic energy budgets in the 16 3D-3C experiments of table 2 and figures 10, 11. The axes, black squares and solid blue stars are identical to those in figure 11. The empty blue stars and the blue asterisks show the two-dimensional and three-dimensional decomposition. Green triangles represent the rate of transfer of K^{2d} to K^{3d}. Orange circles represent the proxy for $\langle S^{3d}\rangle_t$ and $\langle T\rangle_t$ (see (6.7)) and the dashed orange line represents its trend.

(iv) For $\theta Re > 100$ (power throughput >6.25) the transition to a sustained T regime has a straightforward explanation: a fully turbulent flow that sustains high values of S^{3d} in time and space will achieve higher time and volume averages of $\langle S^{3d}\rangle_t$ than an intermittently turbulent flow.

6.3. *Experimental validation*

We plot the time-averaged fluxes of the K^{2d}, K^{3d} budgets in our 16 3D-3C experiments in figure 14. This figure is very similar to figure 11, but shows the $S^{2d}+S^{3d}$ decomposition and the transfer term T.

We observe that $\langle S^{2d}\rangle_t$ dominates in the L and H regimes. To mitigate our underestimation of $\langle S^{3d}\rangle_t$ in the I and T regimes (owing to the computation of small-scale velocity gradients, see § 5.3), we further consider and plot the following proxy:

$$\langle S^{3d}_{proxy}\rangle_t = \langle T_{proxy}\rangle_t \equiv \frac{Re}{2}\langle B_x\rangle_t - \langle S^{2d}\rangle_t. \tag{6.7}$$

This proxy for the three-dimensional energy dissipation and transfer is trustworthy because it relies on the (verified) steadiness of the kinetic energy reservoirs and does not involve computation of small-scale gradients.

We observe in figure 14 that this proxy for the three-dimensional dissipation dramatically increases in an approximately linear fashion above a threshold $\theta Re \approx 40$, shortly before the H → I transition at $\theta Re = 50$ (see trend indicated by the dashed line).

This observation is a key experimental result of this paper and supports the prediction of § 6.2 and figure 13 that the I and T regime correspond to marked increase in three-dimensional dissipation that scales linearly with the power throughput θRe due to the upper bound set on the two-dimensional dissipation by hydraulic controls.

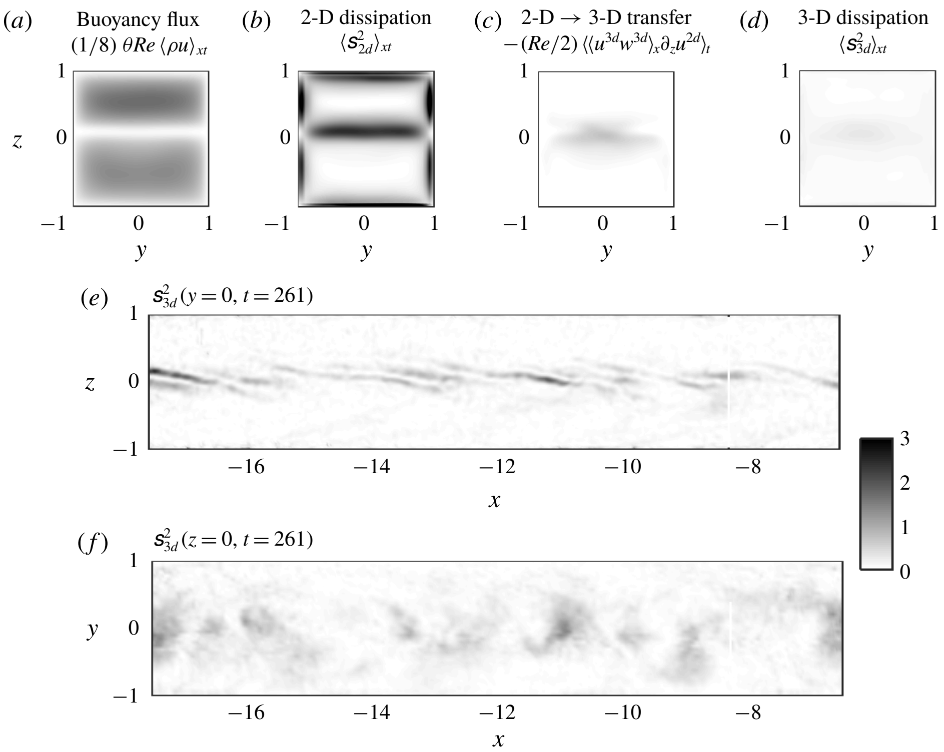

FIGURE 15. Spatial structure of the kinetic energy fluxes in the H regime, whose volume-averaged energetics are sketched in figure 13(*a*). Two-dimensional (2-D) cross-sectional structure of the t- and x-averaged (*a*) horizontal buoyancy flux; (*b*) two-dimensional dissipation, (*c*) $\mathcal{K}^{2d} \rightarrow \mathcal{K}^{3d}$ transfer; (*d*) three-dimensional (3-D) dissipation. Instantaneous three-dimensional dissipation in (*e*) in the vertical mid-plane $y=0$ and (*f*) in the horizontal mid-plane $z=0$. This is the same experiment H1 as in figure 3(*a*–*f*) (instantaneous snapshots are taken at the same arbitrary time $t=261$).

This observation also supports HYP-1 in § 6.2 that Holmboe waves are energetically insignificant and caused by a linear instability triggered by the increased interfacial shear $|\partial_z u|$ reaching a threshold value when $\langle S^{2d}\rangle_t \approx 20$ at the L → H transition (compare the mean profiles between panels f and l in figure 3). To further support HYP-1, we confirmed that the two-dimensional mean flow in experiment L1 ($\langle u\rangle_{x,t}(y, z)$ and $\langle \rho\rangle_{x,y,t}(z)$) was indeed linearly stable to three-dimensional perturbations of the form $\phi' = \hat{\phi}(y, z)\exp(\mathrm{i}kx + \sigma t)$ (using the analysis described in LPZCDL18 § 5.1, which they performed on experiment H4).

6.4. *Spatial structure of energy dissipation*

In this section, we examine the spatial distribution of energy fluxes to reveal information hitherto hidden by volume averaging. In figures 15 and 16, we compare and contrast, for the H1 and T2 experiments respectively, the cross-sectional distribution of the buoyancy flux (panel *a*), two-dimensional dissipation (panel *b*), transfer (panel *c*) and three-dimensional dissipation (panel *d*). The cross-sectional average of the data in each panel respectively yields $(Re/2)\langle B_x\rangle_t$, $\langle S^{2d}\rangle_t$, $\langle T\rangle_t$, $\langle S^{3d}\rangle_t$.

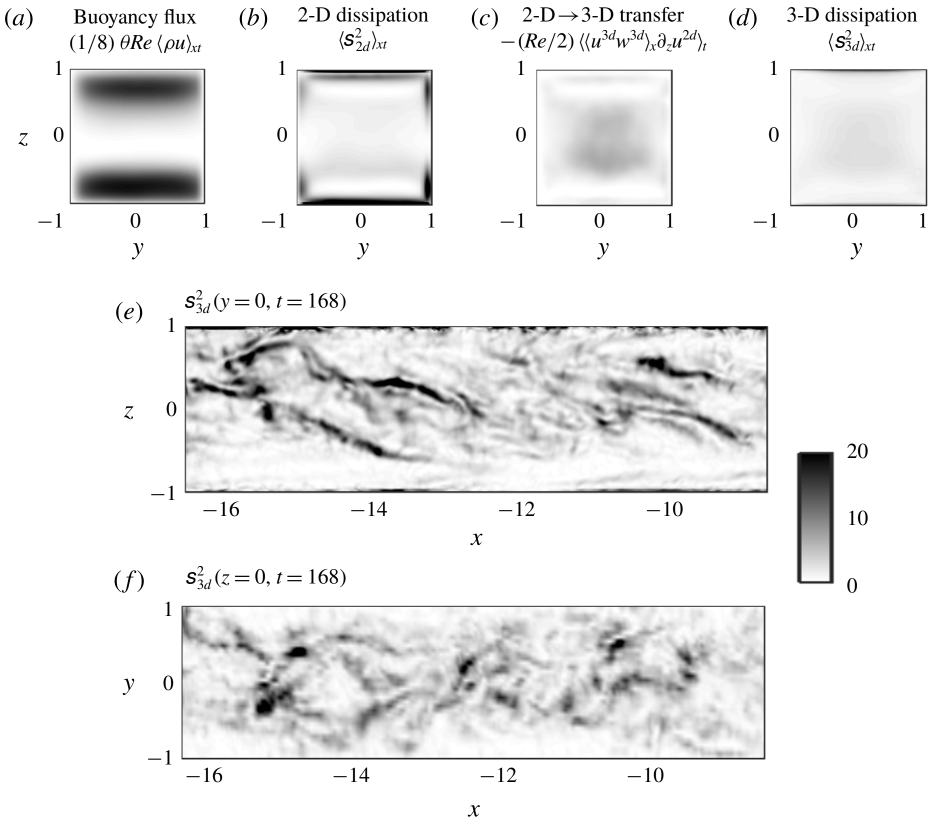

FIGURE 16. Spatial structure of the kinetic energy fluxes in the T regime, whose volume-averaged energetics are sketched in figure 13(*b*). Same panels and legend as figure 15 for side-by-side comparison. This is the same experiment T2 as in figure 4(*g*–*l*) (instantaneous snapshots are taken at the same arbitrary time $t=168$).

We also plot instantaneous snapshots of three-dimensional dissipation in the vertical mid-plane $y=0$ (panel *e*) and horizontal mid-plane $z=0$ (panel *f*) at the same times as the snapshots in figures 3(*a*–*d*) and 3(*g*–*l*). We recall that the volume-averaged transfer and three-dimensional dissipation are underestimated in the T experiment, as can be seen in figure 14 (next-to-rightmost data series). The proxy data in the latter figure suggest that the (averaged) transfer in figure 16(*c*) should be 25 % larger, and the (averaged) dissipation in figure 16(*d*–*f*) should be 50 % larger. The time- and volume-averaged power input $(Re/2)\langle B_x\rangle_t$ (which should equal the total $\langle S^{2d}\rangle_t + \langle S^{3d}\rangle_t$) can be read on figure 14 as ≈ 1 (H1 experiment) and ≈ 7 (T2 experiment). Accordingly, the colour bar in figures 15 and 16 (identical for the all panels of each figure) have respective limits of 3 and 20, equal to about three times the average energy input, allowing for side-by-side comparison of the relative importance of each flux in each regime. Complementary visualisations of slices and averages of the density, velocity and enstrophy fields of experiments H1 (same as in figure 15) and T3 (similar to figure 16) are available in Partridge *et al.* (2019).

In both experiments, the power input (panels *a*) is relatively uniformly distributed within each counter-flowing layer, and low around the sharp interface (H regime, figure 15) and mixing layer (T regime, figure 16). In contrast, the two-dimensional dissipation (panels *b*) is highly localised at the four duct walls, as well as at the interface in the H regime only (in the T regime the interfacial shear is comparatively low). The transfer term (panels *c*) is also highly localised but in the 'active core' of the flow, i.e. at the interface (H) or within the mixing layer (T). This localised power input of $\mathcal{K}^{3d}$ is then dissipated by three-dimensional motions preferentially in the interior (panels *d*) as well as a very close to the top and bottom walls in the T regime. We also observe that the three-dimensional dissipation is more uniform than the transfer in the cross-section. This suggests complex energy transfer pathways and supports the general conclusion that all the kinetic energy fluxes have very different cross-sectional structures, both in the H regime and in the T regime. Next, we focus on the instantaneous snapshots of three-dimensional dissipation in panels (*e*,*f*). Beyond the observation that its volume-average S^{3d} is only significant in the T regime, we see, without surprise, that its spatial structure is highly heterogeneous. 'Wispy' regions with considerable three-dimensional structure feature much enhanced dissipation, several times larger than their respective volume average, especially in the T regime where it locally exceeds the limit of the colour bar.

6.5. *Link with the buoyancy Reynolds number*

The stratified turbulence literature highlights the importance of the buoyancy Reynolds number, defined by scaling analysis of the momentum equations as $Re_b \equiv ReF_h^2$, where F_h is a horizontal Froude number (Brethouwer *et al.* 2007). Strongly stratified turbulence, in which there is a significant range of scales not affected by viscosity, requires $Re_b \gg 1$. However, this definition of Re_b requires the identification of a horizontal length scale ℓ_h to construct F_h which is not obvious in the SID. ML14 estimated $Re_b \approx Re(\ell_h/\ell_v)^2 \approx 10^4(10^{-1})^2 \approx 100$ in their most turbulent SID experiments at $Re = O(10^4)$ using an estimation of the horizontal to vertical length scale ratio of $\ell_h/\ell_v \approx 10$, meant to characterise the elongated turbulent structures visible in the shadowgraphs. Following this approach, we estimate $Re_b = O(10)$ in our most turbulent 3D-3C experiment at $Re = O(10^3)$.

A related definition of Re_b is

$$Re_b \equiv \frac{\epsilon_0}{\nu N_0^2}, \tag{6.8}$$

where the quantities on the right-hand side are dimensional: ϵ_0 is a 'characteristic' rate of turbulent dissipation and N_0^2 is a 'characteristic' value of the buoyancy frequency $N^2 \equiv -(g/\rho_0)\partial_z\rho$. This definition is based on the assumption that $\epsilon_0 \sim q^3/l_h$, where q is a measure of the turbulence intensity. This parameter Re_b is also referred to as the 'activity parameter' and quantifies the separation between the Ozmidov and Kolmogorov length scales (Gibson 1980; Smyth & Moum 2000). Consensus has emerged that $Re_b \gtrsim 20-30$ is required for the flow to have a wide enough range of scales that are not significantly affected either by stratification or by viscosity and hence exhibit the key characteristics of stratified turbulence (Bartello & Tobias 2013). In our recent publication (Lefauve *et al.* 2018, §§ 2.3.2 and 3.2) we quantified Re_b in (6.8) using simple scaling arguments and proposed $Re_b \approx \theta Re$, remarking that the H → I and I → T transitions occurred respectively at $Re_b \approx 50$ and 100.

However, the latter estimates were based on scaling laws which do not accurately represent the quantitative relations involved. The results of this paper on the energetics of SID flows now allow us to provide a more accurate estimate of Re_b as

$$Re_b \approx \frac{2\langle S^{3d}\rangle_t}{\langle|\partial_z\rho|\rangle_{x,y,z,t}} \approx 2\langle S^{3d}\rangle_t. \tag{6.9}$$

The first approximation comes from our non-dimensionalisation of (6.8) and our interpretation of 'characteristic' dissipation and buoyancy frequency as 'time and volume averaged', and of 'turbulent' as 'three-dimensional'. The second approximation comes from $\langle \partial_z \rho \rangle_{x,y,z,t} \approx 1$ since $\langle |\partial_z \rho| \rangle_z = |\rho(z=1) - \rho(z=-1)|/2 = 1$. As we have seen in figure 14, S^{3d}_{proxy} starts increasing shortly before the I → T transition, and grows approximately linearly in the I and T regime. Assuming two-dimensional dissipation would plateau in very turbulent flows (far above the I → T transition), our corollary (4.25) yields

$$Re_b \to \tfrac{1}{8}\theta Re \quad \text{for } \theta Re \gg 100. \tag{6.10}$$

The maximum value achieved in our T experiments is however well below this asymptotic estimate: $Re_b \approx 2S^{3d}_{proxy} \approx 6$ (figure 14, experiment T3, $\theta Re = 132 \not\gg 100$). We note that this value depends on the choice of volume over which the three-dimensional dissipation is averaged, which varies between studies in the literature. If instead of choosing the whole measurement volume delimited by the four duct walls, as we do in (6.9), we chose a smaller volume containing the 'core' of the mixing layer where s^2_{3d} is largest (e.g. $|y|, |z| \leqslant 1/2$), we would obtain an (perhaps more sensible) estimate a factor of 2 to 4 higher, i.e. of magnitude $Re_b = O(10)$. This is about an order of magnitude lower than the values claimed by ML14, because the spatio-temporal resolution constraints of our 3D-3C experiments limit us to flows just above the I → T transition (at $\theta Re = O(100)$, giving $Re_b = O(10)$), whereas some of the shadowgraph observations in ML14 were done much further away from this transition (at $\theta Re = O(10^3)$, giving $Re_b = O(100)$).

7. Conclusions

7.1. *Summary*

In this paper, we investigated the transition in the long-term qualitative behaviour, or flow regime, of geophysically relevant sustained stratified shear flows as two key forcing parameters are varied. We performed laboratory experiments in the stratified inclined duct (SID) set-up (figure 1) which features four qualitatively different regimes: laminar (L), Holmboe waves (H), intermittently turbulent (I) and fully turbulent (T), with increasing three-dimensionality and mixing intensity (figures 3–4 and table 1). These regimes occupy distinct regions in the two-dimensional space of non-dimensional input parameters: duct tilt angle $\theta \in [-1^\circ, 6^\circ]$ and Reynolds number $Re \in [300, 5000]$ (figure 2). Although these regimes have been observed since at least Macagno & Rouse (1961), we argued that previous attempts to explain their transitions were unsuccessful. Although Meyer & Linden (2014) recognised the importance of both θ or Re, their empirical scaling of iso-regime curves scaling with the non-dimensional group θRe^2 does not agree with our new regime diagram obtained in a smaller duct (figure 2). This motivated our search for a scaling law backed by quantitative experimental data and sound physical principles.

Therefore, we derived from first principles evolution equations for the volume-averaged potential and kinetic energy in a control volume of arbitrary length, whose cross-section is bounded by the four walls of our square duct (equations (4.10), (4.13), sketched in figure 5). We then introduced a simplified two-layer frictional hydraulics model (figure 6) to make modelling progress and simplify the energy budgets in SID flows. We distinguished between, on one hand, 'lazy flows' at low $|\theta| \lesssim 2^\circ$, in which the forcing is primarily hydrostatic and dwarfed by viscous friction; and on the other hand, ‘forced flows’, at high $\theta \gtrsim 2^\circ$, in which the forcing is primarily gravitational and is closely balanced by viscous friction (figure 7). We showed that these flows have different energetics (figure 8) and that, in a statistically steady sense (averaged over sufficiently long times), any control volume of a forced flow exhibits simple energy budgets characterised by a single potential power input from the exterior, a single potential-to-kinetic conversion power and a single kinetic dissipation power, all equal in magnitude (equation (4.21) and figure 8*b*). This led us to propose the physical hypothesis that regime transitions are caused by increasing values of the suitably rescaled time- and volume-averaged rate of kinetic energy dissipation, or square norm of the strain rate tensor $\langle \mathsf{s}_{ij}\mathsf{s}_{ij}\rangle_{x,y,z,t}$ (equations (4.22) and (4.23)), and to deduce the ‘forced flow’ corollary that regime transitions should therefore scale like θRe.

We validated this theory in two ways. First, our experimental regime diagram (figure 9) confirmed the θRe scaling predicted by the corollary. Second, we obtained a comprehensive data set of unprecedented volumetric measurements of the density and three-component velocity fields in 16 experiments spanning all four regimes (table 2 and figures 10, 11). Our time- and volume-averaged measurements of all energy fluxes confidently support our theoretical ‘forced flow’ energy budget model, as well as the above physical hypothesis, despite the experimental challenges of obtaining accurate kinetic energy dissipation rates (figure 12).

We delved deeper into the above hypothesis by deriving budgets for the two-dimensional (streamwise-invariant) and three-dimensional components of kinetic energy for forced flows (6.5). We further hypothesised that flows with low power throughput and thus low dissipation power (low θRe, figure 13*a*) are able to dissipate energy exclusively two-dimensionally by increasing the magnitude of the exchange flow rate (volume flux) and their streamwise-invariant wall and interfacial shear (L and H regimes). By contrast, flows with high power throughput (high θRe, figure 13*b*) are not be able to dissipate enough energy two-dimensionally due to the upper limit on the exchange flow rate set by hydraulic control, and thus have to transition to intermittently and fully turbulent regimes with increasingly three-dimensional dissipation scaling with θRe. We validated this hypothesis with our volumetric experimental data set (figure 14) despite having to use indirect evidence (6.7) to mitigate the experimental under-estimation of three-dimensional dissipation. Based on further observations, we suggested that (i) the L → H transition was caused by a Holmboe instability triggered by the increasing interfacial shear resulting from the two-dimensional dissipation scaling with θRe; (ii) the H → I transition might be triggered by another primary instability of the base flow rather than by ever-growing Holmboe waves since the latter are energetically insignificant. We also showed that energy transfers in the three-dimensional experimental volume were complex and heterogeneous in space, particularly in the more turbulent regimes (figures 15 and 16). Finally, we provided a quantitative estimate of the buoyancy Reynolds number (6.9)–(6.10) in the turbulent regime.

To conclude, we believe that we have achieved our initial aim, since our results provide the first mutually consistent physical basis and quantitative experimental data to explain the observed transitions in the different qualitative long-term dynamics of SID flows. The generality of these results provides a useful basis for the study of a broader range of sustained stratified shear flows found in nature.

7.2. *Unanswered questions*

Our results raise at least four unanswered questions:

(i) What is the dynamical explanation for the I → T transition? We proposed that the L → H and H → I transitions were caused by stratified shear instabilities resulting from modifications in the parallel base flow slaved to the energy throughput θRe. We explained that, energetically, sustained turbulence in the T regime was able to achieve higher time-averaged three-dimensional dissipation than intermittently in the I regime. However, does this transition occur by a gradual lengthening of the period of turbulent events with respect to laminar events or by a more abrupt bifurcation? In other words, do 'intermediate' solutions exist with a range of turbulent/laminar period ratios or a range of different dissipative structures? The dynamical details of the transition between intermittency and sustained turbulence, and the quantitative explanation for the transition occurring at $\theta Re \approx 50$ remain open questions.

(ii) How to explain flow regime transitions in horizontal ducts or duct inclined at a slightly negative angle? We indeed observed Holmboe waves and intermittent turbulence for $\theta = 0^\circ$ (figure 2), yet our forced flow scaling of transitions with θRe only applies for $\theta \gtrsim \alpha$ (we recall that $\alpha \equiv H/L$ is the inverse aspect ratio of the duct, see (4.18)). Flows at $|\theta| \lesssim \alpha$ have more complex energetics (figure 8*a*), and we have seen that, in such flows, transitions appear to scale with θRe^2 instead of θRe (figure 9). Further work is needed to understand lazy flow dynamics and explain this θRe^2 scaling.

(iii) Why did ML14 observe a different transition scaling in a different duct geometry? As evidenced by the dashed line in figure 2 and as discussed in § 2.5, their experiments in a duct with a larger cross-section ($H = 100$ mm versus 45 mm in this paper) suggested a θRe^2 scaling (both for lazy and forced flows) in disagreement with our theory. However, we note that the Reynolds numbers in ML14 are typically larger than ours. At sufficiently large Re, wall boundary layers are not fully developed, i.e. they do not span the whole cross-section of the duct, as was typically the case in the data shown in this paper. Instead, wall boundary layers become sufficiently thin that the volume-averaged contribution of wall dissipation is no longer of order 1 but scales with $Re^{1/2}$. This apparently undermines our simple hypothesis (4.23) that increasingly turbulent regimes correspond to increasing values of the volume-averaged dissipation well above 'laminar' $O(1)$ values, but more work is required to investigate this question.

(iv) What is the role of mixing? In this paper, we focused on kinetic energy dissipation to explain regime transitions and did not explicitly derive or represent irreversible mixing in the energy budgets. Irreversible mixing is implicitly accounted for in the mass flux Q_m (3.3), to which the energy throughput of forced flows is proportional (see (4.24)). Although the black contours in figure 9 show that the mass flux has a complicated $Q_m(\theta, Re)$ dependence (due primarily to the volume flux $Q(\theta, Re)$ and secondarily to mixing), we made the reasonable assumption that, in forced flows, $Q \approx Q_m \approx 0.5$ (leading to (4.25)). We believe that neglecting mixing in this fashion is acceptable for the work in this paper, but acknowledge that a better understanding of the $Q(\theta, Re)$ and $Q_m(\theta, Re)$ relations is desirable. More generally, beyond the Q_m/Q question and its (moderate) impact for the energy throughput in forced flow, we believe that the study of mixing and mixing efficiency in sustained stratified shear flows remains a major research objective. However we are currently not able to measure mixing accurately in experiments; the Batchelor length scale is typically $Sc^{1/2} \approx 25$ times smaller than the Kolmogorov scale, which is already challenging to resolve (§ 5.3). For a more detailed discussion of mixing in the SID experiment, see Lefauve (2018) § 6.7.

Acknowledgements

A.L. is funded by an Engineering and Physical Sciences Research Council (EPSRC) Doctoral Prize Fellowship. All authors acknowledge funding from the EPSRC under the Programme Grant EP/K034529/1 ‘Mathematical Underpinnings of Stratified Turbulence’ (MUST), and from the European Research Council (ERC) under the European Union’s Horizon 2020 research and innovation programme under grant no. 742480 ‘Stratified Turbulence And Mixing Processes’ (STAMP). We thank the ‘MUST team’ in DAMTP for helpful discussions and especially Professor C. P. Caulfield about the two-dimensional/three-dimensional decomposition. We are grateful for the invaluable experimental support of Professor S. B. Dalziel and of the technicians of the G. K. Batchelor Laboratory. The data associated with this paper can be downloaded from the repository https://doi.org/10.17863/CAM.41410.

Appendix A. Experimental constraints

The physical constraints currently limiting the resolution and temporal duration of our experimental measurements are as follows:

(i) The streamwise and vertical resolutions $\Delta x \equiv \ell/n_x$, $\Delta z \equiv 2/n_z$ (where n_x, n_z are the number of sPIV vectors in each direction) are generally equal and limited by the resolution of the cameras, by the size of the PIV particles (typically 50 μm) and by their seeding density. Using 8 MPixel cameras, 31×31 Pixel interrogation windows, a 75 % overlap, and volumes of length $\ell \approx 11$, we typically obtained $n_x \approx 500$, $n_z \approx 100$, i.e. $\Delta x \approx \Delta z \approx 0.02$. Density data were obtained at higher resolution because of the absence of interrogation windows in PLIF, but since this higher resolution was not needed for the analysis in this paper, they were smoothed before being interpolated onto the grid of the velocity data.

(ii) The spanwise resolution $\Delta y \equiv 2/n_y$ is limited by the finite thickness of our laser sheet (required for sPIV measurements) estimated to be ≈1.5 mm $\approx H/30$, dictating $n_y \approx 30 - 40$ as a good compromise to avoid excessive redundancy of overlapping laser sheets, and therefore a typical resolution $\Delta y \approx 0.05 - 0.07$ (coarser than Δx, Δz).

(iii) The temporal resolution $\Delta t \equiv n_y \delta t$ of our measurements is primarily limited by the previously set n_y and the laser frequency of δt^{-1} (a maximum of 100 Hz in dimensional units, i.e. 100 double pulses per second). This results in a typical non-dimensional lower bound $\Delta t \gtrsim 30 \times 100^{-1} \times \Delta U/H = (1.2\nu/H^2)Re \approx Re/1600$, making the near-instantaneous ‘freezing’ of volumes better (i.e. Δt smaller) in low-Re flows than in high-Re flows (for a given H and ν). For the flows considered in this paper, $\Delta t \approx 1 - 4$ ATU (the lower bound $\Delta t \approx Re/1600$ was only rarely realised since the laser could only be set at its maximum frequency for the fastest, highest-Re flows).

(iv) The duration of the recorded data, $\tau \equiv n_t \Delta t$, and therefore the number of successive volumes measured n_t, is limited by the available RAM storage memory (50 GB) dedicated to each camera (two cameras for sPIV and one camera for PLIF). A total of 150 GB of raw data typically yielded ≈18 000 frames per camera, i.e. ≈9000 sPIV fields or $n_t = 9000/n_y \approx 300$ volumes spanning a duration $\tau \approx 10^2 - 10^3$ ATU (typically a few minutes). Although τ is typically shorter than the maximum duration of an experiment (before the flooding of the controls, determined by the size of the reservoirs), we refer to it as the ‘duration of an experiment’ in this paper for simplicity.

Appendix B. Estimation of energy fluxes

Based on the two-layer hydraulic model of figure 6, we use the definitions for the energy fluxes in the K and P budgets (4.4), (4.5), (4.8) to estimate the following (derivations can be found in L18, § 6.3.1):

(i) The advective boundary flux K is

$$\Phi_K^{adv} = -\frac{Q^3}{\ell}\left\{\frac{\eta_L}{(1-\eta_L^2)^2} - \frac{\eta_R}{(1-\eta_R^2)^2}\right\} \leqslant 0 \quad \text{since } \eta_L \geqslant \eta_R, \tag{B 1}$$

it is thus always negative (it acts as a sink to K) since the interface must slope down. In other words, the inflow of kinetic energy in V by the velocities u_{1L}, u_{2R} is always smaller than the outflow by the velocities u_{2L}, u_{1R}. (Note that even more negative Φ_K^{adv} would be obtained by relaxing the assumption of uniform flow in each layer and taking into account the non-unitary velocity distribution coefficient when evaluating $\langle u^3\rangle_{y,z}$, which is typically greater for the thin outflowing layers than for the thick inflowing layers).

Importantly, we note that $\Phi_K^{adv} = 0$ if V is approximately periodic in x, i.e. if velocities and interface position are identical at the left and right boundaries. For any general V, this requires that the interface is flat everywhere $\eta(x) = 0$, which as explained in § 4.3.1 corresponds to forced flows guaranteed at large tilt angles $\theta > \alpha$.

(ii) The pressure boundary flux of K is

$$\Phi_K^{pre} = \frac{1}{4\ell}\langle u(\eta - z)\rangle_{y,z}|_{L-R} = 0, \tag{B 2}$$

under the assumptions of no barotropic flow $\langle u\rangle_{x,y,z} = 0$ and of hydrostatic flow (in particular that u does not depend on z). We will therefore neglect this flux.

(iii) The viscous boundary flux of K is

$$\Phi_K^{vis} = \frac{8Q^2}{\ell\, Re}\left\{\frac{\eta_L\eta_L'}{(1-\eta_L^2)^2} - \frac{\eta_R\eta_R'}{(1-\eta_R^2)^2}\right\}. \tag{B 3}$$

We note that, similarly to the advective flux, $\Phi_K^{vis} = 0$ in forced flows (i.e. if V is periodic). However, for the large $Re \gg 1$ investigated here, this flux will be neglected compared to the advective flux $|\Phi_K^{vis}| \ll |\Phi_K^{adv}|$.

(iv) The advective boundary flux of P is

$$\Phi_P^{adv} = \underbrace{\frac{1}{4\ell}Q_m\left(\frac{\eta_L}{1-\eta_L^2} - \frac{\eta_R}{1-\eta_R^2}\right)}_{\substack{\text{hydrostatic} \\ \text{forcing}}>0} + \underbrace{\frac{1}{4}Q_m\theta}_{\substack{\text{gravitational} \\ \text{forcing}}>0} > 0. \tag{B 4}$$

We note that Φ_P^{adv} has two distinct positive components: hydrostatic forcing and gravitational forcing, as already identified in (4.17). Consistently with the discussion of § 4.3.1, we see here that for forced flows the hydrostatic term cancels and only the gravitational forcing remains.

(v) The diffusive boundary flux of P

$$\Phi_P^{dif} = \frac{1}{4\ell\, Re\, Sc}\left[\theta\left\{\left(\bar{x} + \frac{\ell}{2}\right)\eta_R' - \left(\bar{x} - \frac{\ell}{2}\right)\eta_L'\right\} + (\eta_L\eta_L' - \eta_R\eta_R')\right], \tag{B 5}$$

where again, $\Phi_P^{dif} = 0$ for forced flows. Moreover, just like Φ_K^{vis}, we neglect this flux for the large Re and Sc used here since $|\Phi_P^{dif}| \ll |\Phi_P^{adv}|$.

(vi) The horizontal buoyancy flux

$$B_x = \tfrac{1}{4}\langle \rho u\rangle_{x,y,z}\,\theta = \tfrac{1}{4}Q_m\,\theta > 0, \tag{B 6}$$

which is exactly equal to the gravitational component of $\varPhi_P^{adv}$ (see (B 4)).

(vii) The vertical boundary flux

$$B_z = -Q_m\frac{\eta_L-\eta_R}{4\ell} \leqslant 0, \tag{B 7}$$

under the assumption that the centre of mass of a slab of dense ($\rho = 1$) fluid drops by $\eta_L - \eta_R$ over the length ℓ (i.e. it has a negative vertical velocity), and conversely for a slab of buoyant ($\rho = -1$) fluid. In the absence of any other vertical motion other than those consistent with hydraulic theory, it is thus negative, meaning that it acts as a source term for K (where it appears as $-B_z$, see (4.10)) and as a sink for P (where it appears as $+B_z$, see (4.13)). We note that this flux also cancels for forced flows. However, if we relax the hydraulic assumptions (as will be required to investigate the laboratory flows in this paper), non-trivial vertical motions (turbulence) may render B_z sign indefinite. We therefore consider this flux to be irreversible (negative definite) in flows close to the hydraulic assumptions (L and H regimes) and potentially reversible (sign indefinite) in flows where vertical motions may be large (I and T regimes).

(viii) The conversion of I to P

$$\varPhi_P^{int} = \frac{1}{4\,Re\,Sc}\left\{-\underbrace{\frac{\eta_L-\eta_R}{\ell}\,\theta}_{>0\ and\ \ll 1} + 1\right\} \approx \frac{1}{4\,Re\,Sc}, \tag{B 8}$$

since $\langle\rho\rangle_{y,z} = \eta$, by definition of η, assuming collocation of the velocity and density interfaces, and $\langle\rho\rangle_{x,y}|_{B-T} = 1-(-1) = 2$. Given the large Re and Sc investigated here, we neglect it.

(ix) The viscous dissipation: under the assumptions of hydraulic theory, $D = 0$. When relaxing these assumptions, $D > 0$ but is *a priori* unknown (though we show in § 4.3 that it can be deduced in the simplified budget of forced flows).

REFERENCES

ARMI, L. 1986 The hydraulics of two flowing layers with different densities. *J. Fluid Mech.* **163**, 27–58.

ARMI, L. & FARMER, D. M. 1988 The flow of Mediterranean water through the Strait of Gibraltar. *Prog. Oceanogr.* **21**, 1–105.

BARTELLO, P. & TOBIAS, S. M. 2013 Sensitivity of stratified turbulence to the buoyancy Reynolds number. *J. Fluid Mech.* **725**, 1–22.

BRETHOUWER, G., BILLANT, P., LINDBORG, E. & CHOMAZ, J.-M. 2007 Scaling analysis and simulation of strongly stratified turbulent flows. *J. Fluid Mech.* **585**, 343–368.

CAULFIELD, C. P. & PELTIER, W. R. 2000 The anatomy of the mixing transition in homogeneous and stratified free shear layers. *J. Fluid Mech.* **413**, 1–47.

FARMER, D. & ARMI, L. 1999 Stratified flow over topography: the role of small-scale entrainment and mixing. *Proc. R. Soc. Math., Phys. Engng Sci.* **455**, 3221–3258.

FERNANDO, H. J. S. 1991 Turbulent mixing in stratified fluids. *Annu. Rev. Fluid Mech.* **23** (1), 455–493.

GEYER, W. R., LAVERY, A. C., SCULLY, M. E. & TROWBRIDGE, J. H. 2010 Mixing by shear instability at high Reynolds number. *Geophys. Res. Lett.* **37** (22), L22607.

GIBSON, C. H. 1980 Fossil temperature, salinity, and vorticity turbulence in the ocean. In *Marine Turbulence* (ed. J. Nihoul), pp. 221–257. Elsevier.

GREGG, M. C., D'ASARO, E. A., RILEY, J. J. & KUNZE, E. 2018 Mixing efficiency in the ocean. *Annu. Rev. Mar. Sci.* (10), 443–473.

GREGG, M. C., PETERS, H., WESSON, J. C., OAKEY, N. S. & SHAW, T. J. 1985 Intensive measurements of turbulence and shear in the equatorial undercurrent. *Nature* **318**, 140–144.

GU, L. 2001 Frictional exchange flow through a wide channel with application to the Burlington ship canal. PhD thesis, The University of British Columbia.

GU, L. & LAWRENCE, G. A. 2005 Analytical solution for maximal frictional two-layer exchange flow. *J. Fluid Mech.* **543**, 1–17.

VAN HAREN, H., GOSTIAUX, L., MOROZOV, E. & TARAKANOV, R. 2014 Extremely long Kelvin–Helmholtz billow trains in the Romanche Fracture Zone. *Geophys. Res. Lett.* **41** (23), 8445–8451.

IVEY, G. N., WINTERS, K. B. & KOSEFF, J. R. 2008 Density stratification, turbulence, but how much mixing? *Annu. Rev. Fluid Mech.* **40** (1), 169–184.

KIEL, D. E. 1991 Buoyancy driven counterflow and interfacial mixing. PhD thesis, University of Cambridge.

LAWRENCE, G. A. 1990 On the hydraulics of Boussinesq and non-Boussinesq two-layer flows. *J. Fluid Mech.* **215**, 457–480.

LEFAUVE, A. 2018 Waves and turbulence in sustained stratified shear flows. PhD thesis, University of Cambridge. doi:10.17863/CAM.24648.

LEFAUVE, A., PARTRIDGE, J. L., ZHOU, Q., CAULFIELD, C. P., DALZIEL, S. B. & LINDEN, P. F. 2018 The structure and origin of confined Holmboe waves. *J. Fluid Mech.* **848**, 508–544.

LINDEN, P. F. 1979 Mixing in stratified fluids. *Geophys. Astrophys. Fluid Dyn.* **13** (1), 3–23.

MACAGNO, E. O. & ROUSE, H. 1961 Interfacial mixing in stratified flow. *J. Engng Mech. ASCE* **87** (EM5), 55–81.

MAHRT, L. 2014 Stably stratified atmospheric boundary layers. *Annu. Rev. Fluid Mech.* **46** (1), 23–45.

MASHAYEK, A., CAULFIELD, C. P. & PELTIER, W. R. 2013 Time-dependent, non-monotonic mixing in stratified turbulent shear flows: implications for oceanographic estimates of buoyancy flux. *J. Fluid Mech.* **736**, 570–593.

MASHAYEK, A. & PELTIER, W. R. 2012*a* The 'zoo' of secondary instabilities precursory to stratified shear flow transition. Part 1. Shear aligned convection, pairing, and braid instabilities. *J. Fluid Mech.* **708**, 5–44.

MASHAYEK, A. & PELTIER, W. R. 2012*b* The 'zoo' of secondary instabilities precursory to stratified shear flow transition. Part 2. The influence of stratification. *J. Fluid Mech.* **708**, 45–70.

MEYER, C. R. & LINDEN, P. F. 2014 Stratified shear flow: experiments in an inclined duct. *J. Fluid Mech.* **753**, 242–253.

PARTRIDGE, J. L., LEFAUVE, A. & DALZIEL, S. B. 2019 A versatile scanning method for volumetric measurements of velocity and density fields. *Meas. Sci. Technol.* **30**, 055203.

PELTIER, W. R. & CAULFIELD, C. P. 2003 Mixing efficiency in stratified shear flows. *Annu. Rev. Fluid Mech.* **35** (1), 135–167.

SALEHIPOUR, H., PELTIER, W. R. & MASHAYEK, A. 2015 Turbulent diapycnal mixing in stratified shear flows: the influence of Prandtl number on mixing efficiency and transition at high Reynolds number. *J. Fluid Mech.* **773**, 178–223.

SCHIJF, J. B. & SCHÖNFLED, J. C. 1953 Theoretical considerations on the motion of salt and fresh water. In *Proceedings of the Minnesota International Hydraulic Convention*. IAHR.

DE SILVA, C. M., PHILIP, J. & MARUSIC, I. 2013 Minimization of divergence error in volumetric velocity measurements and implications for turbulence statistics. *Exp. Fluids* **54**, 1557.

SMYTH, W. D. & MOUM, J. N. 2000 Length scales of turbulence in stably stratified mixing layers. *Phys. Fluids* **12** (6), 1327–1342.

SMYTH, W. D. & MOUM, J. N. 2013 Marginal instability and deep cycle turbulence in the eastern equatorial Pacific Ocean. *Geophys. Res. Lett.* **40** (23), 6181–6185.

THORPE, S. A. & LIU, Z. 2009 Marginal instability? *J. Phys. Oceanogr.* **39** (9), 2373–2381.

TURNER, J. S. 1973 *Buoyancy Effects in Fluids*. Cambridge University Press.

WANG, C., GAO, Q., WEI, R., LI, T. & WANG, J. 2017 Weighted divergence correction scheme and its fast implementation. *Exp. Fluids* **58**, 44.

WILKINSON, D. L. 1986 Buoyancy driven exchange flow in a horizontal pipe. *J. Engng Mech.* **112** (5), 485–497.

WINTERS, K. B., LOMBARD, P. N., RILEY, J. J. & D'ASARO, E. A. 1995 Available potential energy and mixing in density-stratified fluids. *J. Fluid Mech.* **289**, 115–128.